

FERROELECTRIC AND FERROMAGNETIC BEHAVIOR
OF OXIDE CONTAINING THIN FILMS

by

CHOI HAI IN

Presented to the Faculty of the Graduate School of
The University of Texas at Arlington in Partial Fulfillment
of the Requirements
for the Degree of

MASTER OF SCIENCE IN PHYSICS

THE UNIVERSITY OF TEXAS AT ARLINGTON

MAY 2015

Copyright © by Choi Hai In 2015

All Rights Reserved



Acknowledgements

I would like to express my deepest appreciation and gratitude to my advisors, Professor J. Ping Liu and Won-Jeong Kim, for providing invaluable guidance for my research and for constantly supporting me over the past four years. I especially thank the advisors for introducing me to scientific research and providing me with challenges. Dr. Liu's expertise in magnetism, along with his vision of magnetic material, has been a source of inspiration for me to pursue further research in this field. Dr. Kim's expertise in oxide thin film, along with his vision of ferroelectric and semiconductor, has been a good opportunity for me to understand of pulsed deposition method and further research in this field.

I would also like to express my appreciation to Professor Jae Yu for arranging this unique program with the physics department in both universities. (Changwon National University and University of Texas at Arlington)

Also, I would like to express my appreciation to Professor Yao Hao (exchange bias project from UTA), Tae Kwon Song, Myung-Ho Kim, Sang-Su Kim (ferroelectric thin film project from CNU) for serving as research supervisor. I am grateful to them for their support during my research.

I am indebted to past and present colleagues for their important suggestions, assistance, encouragement of my studies and research, and wonderful friendship during our time together. Among them are Dr. Narayan Poudyal, Dr. Kevin Elkins, Dr. Xubo Liu Kinjal Gandha, Zhao Guo Qiu, Xiaotong Liu in UTA. Also, I am supported from Dr. Myung Hwan Lee, Jin Su Park, Sangwook Kim, Da Jeong Kim, Sung-Jin Han in CNU.

This work was supported by the Changwon National University and University of Texas at Arlington (2013-2015).

May 9, 2015

Abstract

FERROELECTRIC AND FERROMAGNETIC BEHAVIOR
OF OXIDE THIN FILMS

Choi Hai In

The University of Texas at Arlington, 2015

Supervising Professor: J. Ping Liu

Oxide materials are important due to their interesting physical properties for applications in future electronic devices. Thin film oxide materials show a variety of electric and magnetic properties such as ferroelectric, piezoelectric, ferromagnetic and superconducting properties.

One intriguing material, bismuth ferrite, has shown room-temperature multiferroic order. It has ferroelectric order below the 1100 K Curie temperature and large remnant polarization. Also, it has antiferromagnetic order below the Néel temperature of 650 K. However, the bismuth ferrite has several defect-related issues such as bismuth volatilization, transition of iron valence electron states and oxygen vacancies. The multiferroic properties are changed by the defect states of the thin films. In this study, the valence electron transition of iron and oxygen vacancy is investigated.

Exchange bias is one of the important phenomena in magnetic materials. The exchange bias is formed from exchange anisotropy between ferromagnetic and antiferromagnetic materials and observed with field-cooling to temperatures lower than the Néel temperature of the antiferromagnetic material. In thin film materials, the phenomenon is also affected by substrate conditions. In this study, the exchange bias is investigated for Co/CoO bilayer thin films on flat substrates and modulated substrates.

Table of Contents

Acknowledgements	iii
Abstract	iv
List of Illustrations	vii
List of Tables	x
Chapter 1 Introduction.....	1
1.1 Ferroelectricity	1
1.2 Ferromagnetism.....	6
1.3 Antiferromagnetism	9
1.4 Exchange Bias.....	13
Chapter 2 Sample Preparation Methods and Experimental Techniques.....	16
2.1 Sample Preparation Methods	16
2.1.1 Sputtering Method	16
2.1.2 Pulsed Laser Deposition Method	17
2.2 Experimental Techniques	19
2.2.1 X-ray Diffraction (XRD).....	19
2.2.2 Scanning Electron Microscope (SEM).....	19
2.2.3 X-Ray Photoelectron Spectroscopy (XPS).....	20
2.2.4 P-E Hysteresis Loop	20
2.2.5 M-H Hysteresis Loop	20
2.2.6 Leakage Current Density	20
Chapter 3 Ferroelectric and Ferromagnetic Behavior of BiFeO ₃ Thin Films	
with Different Iron Valence Electron State	21
3.1 Sample Preparation of BiFeO ₃ Thin Films.....	21
3.2 Analysis of BiFeO ₃ Thin Films	22

3.2.1 X-ray Diffraction Analysis	22
3.2.2 SEM Analysis	23
3.2.3 X-ray Photoelectron Spectroscopy Analysis	24
3.2.4 P-E Hysteresis Loop Analysis	26
3.2.5 Leakage Current Density Analysis	27
3.2.6 M-H Hysteresis Loop Analysis	30
3.3 Conclusion	31
Chapter 4 Exchange Bias Behavior of Co/CoO Bilayer on Flat and Modulated	
Substrates	32
4.1 Sample Preparation of Co/CoO Thin Films	32
4.2 Analysis of Co/CoO Thin Films.....	33
4.2.1 Exchange Bias Behavior of Co/CoO Bilayer on Flat Substrate	33
4.2.2.1 M-H Hysteresis Loop Analysis	34
4.2.2 Exchange Bias Behavior of Co/CoO Bilayer on Modulated	
Substrate	38
4.2.2.1 Surface and Cross Section Analysis.....	38
4.2.2.2 M-H Hysteresis Loop Analysis	40
Chapter 5 Summary and Conclusion	45
References	47
Biographical Information	52

List of Illustrations

Figure 1-1 ABO_3 type of perovskites.....	3
Figure 1-2 Polarization-electric field hysteresis loops.....	4
Figure 1-3 Degrading behaviors of ferroelectric properties	5
Figure 1-4 3d and 4s up- and down-spin densities of states in first-row transition metals, with exchange interaction included	7
Figure 1-5 Magnetization-magnetic field hysteresis loops.....	8
Figure 1-6 Typical temperature dependence of magnetization curves (Θ =Curie temperature, M_0 =saturated magnetization).....	9
Figure 1-7 Magnetic moment arrangement and (b) two magnetization response depend on external magnetic field of antiferromagnetic materials	10
Figure 1-8 Temperature dependence of susceptibility for antiferromagnetic materials (χ_{\perp} = perpendicular to the magnetic field, χ_{\parallel} = parallel to the magnetic field, and χ_{poly} = polycrystalline sample to the magnetic field)	12
Figure 1-9 Field dependence spin orientation behavior of magnetic hysteresis loop. (i), (ii) saturated point at positive field, (iii) positive to negative field point, (iv) saturated point at negative field, (v) minimized negative field [6]	15
Figure 2-1 Schematic of RF sputtering methods.	16
Figure 2-2 Schematic of PLD methods.....	18
Figure 3-1 XRD patterns of the (a) $BFO(Fe_2O_3)$ and (b) $BFO(Fe_3O_4)$ thin films.....	22
Figure 3-2 FE-SEM images of surface from (a) $BFO(Fe_2O_3)$ and (b) $BFO(Fe_3O_4)$	23
Figure 3-3 XPS spectra of (a) $BFO(Fe_2O_3)$, (b) $BFO(Fe_3O_4)$ in Fe site and (c) $BFO(Fe_2O_3)$, (d) $BFO(Fe_3O_4)$ in O site.	24

Figure 3-4 Ferroelectric hysteresis loops of (a) BFO(Fe_2O_3) and (b) BFO(Fe_3O_4) thin film measured frequency at 10 kHz	26
Figure 3-5 Leakage current density (J) versus electric field (E) of BFO(Fe_2O_3) (black) and BFO(Fe_3O_4) (red) plot in (a) symmetry of negative and positive bias, (b) $\log(J)$ vs linear (E) (c) $\log(J)$ vs $\log(E)$, and $\ln(J/E^2)$ vs $1/E$	27
Figure 3-6 Magnetic hysteresis loops of (a) BFO(Fe_2O_3) and BFO(Fe_3O_4) thin film (b) collected data from (a).	30
Figure 4-1 Magnetic hysteresis loops of Co/CoO bilayer on flat substrate with different Co thicknesses (a) Co=20 nm, (b) Co=12 nm (c) Co=9 nm and (d) Co=7 nm.....	34
Figure 4-2 Co thickness versus exchange bias results	35
Figure 4-3 Training effects of Co/CoO bilayer on flat substrate (a) Co=20 nm, (b) Co=12 nm (c) Co=9 nm and (d) Co=7 nm.....	36
Figure 4-4 Training time versus exchange bias results	37
Figure 4-5 SEM images of surface and cross section of modulated substrate with top view with different scale in (a) and (b), tiled view with different scale in (c) and (d).	38
Figure 4-6 TEM image of cross section of Co/CoO bilayer on modulate substrate	39
Figure 4-7 Calculated magnetic hysteresis loops depend on unbiased magnetization with (a) variety of numerical number, (b) numerical number: 1, (c) numerical number: 0.5 and (d) numerical number: 0	40
Figure 4-8 Magnetic hysteresis loops from Co/CoO bilyer on modulated substrate with different CoO thickness (a) CoO=1 nm, (b) CoO=3 nm, and (c) CoO=4 nm.....	41
Figure 4-9 Calculation and measurement hysteresis loops from Co/CoO bilayer on modulated substrate with numerical number (a) 0.643, (c) 0.4 and thickness of Co and CoO layer (b) 8 and 3 nm, (d) 8 and 4 nm.....	43

Figure 4-10 Magnetic hysteresis loops of Co/CoO=8/1 nm with (a) modulated substrate and (b) flat substrate	44
---	----

List of Tables

Table 1-1 Piezoelectric material classifications	2
--	---

Chapter 1

Introduction

This chapter describes ferroelectricity, ferromagnetism, antiferromagnetism and exchange bias. The physical behavior of ferroelectricity is focused on the structure, ferroelectric hysteresis loop and degradation of ferroelectricity. The basic physical properties of ferromagnetism and antiferromagnetism are discussed, and exchange bias behavior is described based on exchange anisotropy between a ferromagnetic layer and antiferromagnetic layer.

1.1 Ferroelectricity

There are a few materials in the nature that exhibit a spontaneous electric polarization which is reversible when an external electric field is applied. These are called ferroelectrics. The first kind of these materials was discovered in 1920 from Rochelle salt by Valasek. [1] Since then, ferroelectricity was found in many natural and synthetic materials, such as barium titanate, perovskite, and etc. From further investigations on these ferroelectrics, it was found that ferroelectricity come from the crystal symmetry.

Crystals can be defined as a periodic arrangement of the atoms. Based on the mathematical and geometrical analysis, all of the periodic and symmetric arrangement of the atoms in 3-dimensions can be classified into 32 crystallographic point groups.

Among these, 21 groups have non-centrosymmetric centers. Among these 21 groups, 20 have a direct piezoelectric effect. Furthermore, 10 groups out of the 20 piezoelectrics exhibit a spontaneous polarization with temperature dependence. For this reason these 10 groups are called pyroelectrics. Among these 10 pyroelectrics, some crystals exhibit reversible polarization with an externally applied electric field, while others do not. These having an electrically reversible spontaneous polarization are called ferroelectrics.

Table 1.1 Piezoelectric material classifications.

32 Crystalline classes			
20 classes piezoelectric			Non-piezoelectric
10 classes pyroelectric		Non-pyroelectric	
ferroelectric	Non-ferroelectric		
e.g. : BaTiO ₃ , PbTiO ₃	e.g. : Tournaline	e.g. : Quartz	

One famous type of ferroelectrics is the ABO_3 type perovskite structure. The perovskite crystal structure of the ABO_3 type can have a centrosymmetric cubic structure and non-centrosymmetric rhombohedral, orthorhombic, and tetragonal as shown in Figure 1.1. For the ABO_3 structure, A is the atom at the corners, B is near the center of the volume, and O occupies near the center of the face period. Typically, rhombohedral, orthorhombic and tetragonal structures have polarization directions with $\langle 111 \rangle$, $\langle 110 \rangle$, and $\langle 001 \rangle$, respectively. For these 3 non-centrosymmetric structure, the off-center B site ions are distorted to the polarization direction without an external electric field. On the other hand, the cubic structure does not have an off-center B site ions due to the symmetric center structure, which is called paraelectric.

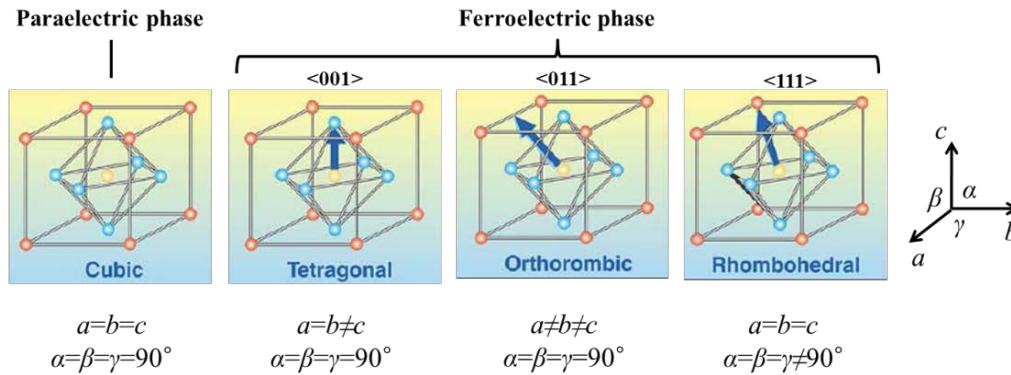


Figure 1.1 ABO_3 type of perovskites.

Ferroelectric materials have a temperature dependent ordering. In a specific temperature region, the centrosymmetric phase (cubic phase) is transformed to non-centrosymmetric phase such as, rhombohedral, orthorhombic, or tetragonal phase. This transition temperature from paraelectric to ferroelectric is called the Curie temperature (T_c).

A defining characteristic of ferroelectric materials comes from the polarization-electric (P-E) field hysteresis loop as shown in Figure 1.2. The polarization is switched by applying an alternating electric field to the ferroelectric material. The spontaneous polarization is defined from the saturated polarization at large value of positive ($+P_s$, $-P_s$). At this state, the ferroelectric domains are aligned to the polarization direction. The remnant polarization is determined from the polarization at zero external electric field. At this state, some ferroelectric domains are back-switched, but the polarization is not zero. To reach the zero polarization state, the field must be reversed. This field value is called the coercive field.

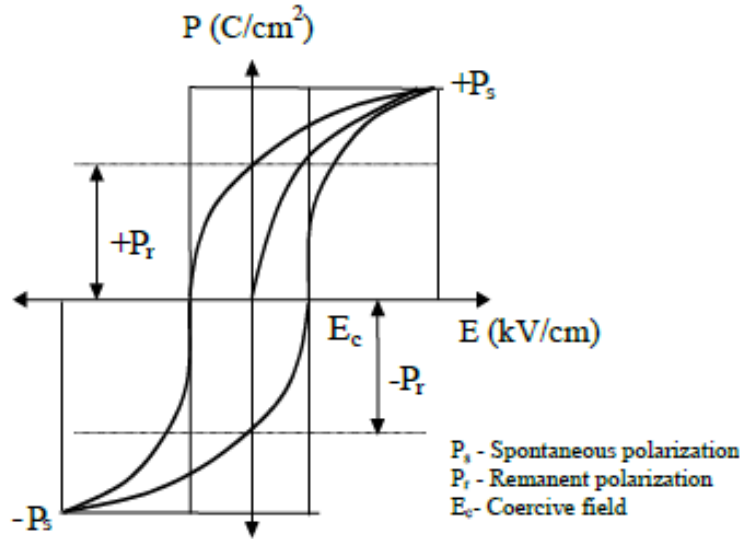


Figure 1.2 Polarization-electric field hysteresis loops.

Figure 1.3 shows the degrading electrical behavior for a ferroelectric hysteresis loop. Fatigue is one of the major problem for ferroelectric thin films, which is observed after cycling the polarization several times (figure 1.3 (a)). Fatigue is characterized by a decrease in the remnant polarization after several cycles when compared to the first loop measurement. Retention loss is another problem in applying ferroelectrics to memory devises. In retention loss, the P_r decreases if the ferroelectric is not switched frequently in an external electric field (Figure 1.3 (b)). This behavior is similar to fatigue but the difference between switching and non-switching dipoles become smaller. Imprint is another effect that degrades the property of a ferroelectric material. This occurs when the ferroelectric film is measured at a high electric field or repeated unipolar pulses for a long time. After imprinting the polarization is not fully saturated by an applied single electric field pulse with the opposite polarity (Figure 1.3 (c)). This kind of behavior is observed in

lead based ferroelectric materials or bismuth based ferroelectric materials. Leakage current behavior is the last problem for ferroelectric materials (Figure 1.3 (d)). Although the dielectric material is an insulator, defects are easily formed at grain boundary with atomic vacancies which allows free electrons to flow into the material between the electrodes. This defect will give rise to a current path.

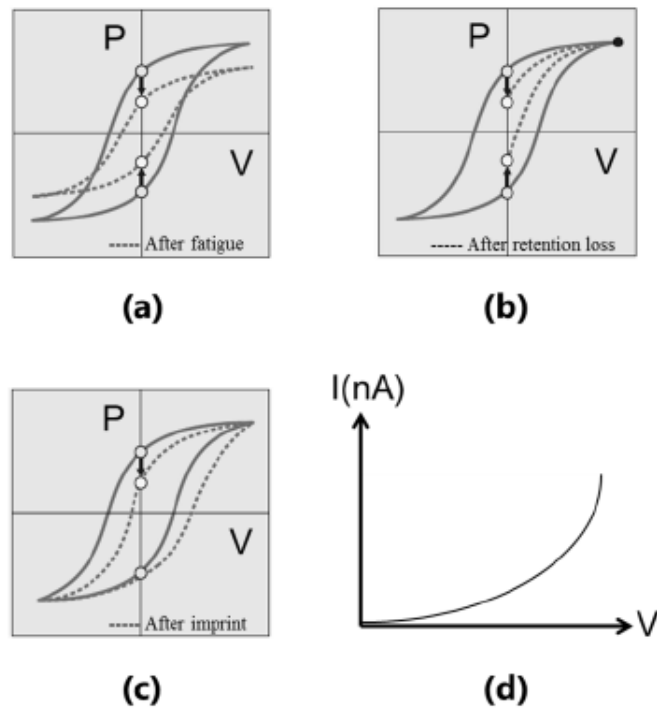


Figure 1.3 Degrading behaviors of ferroelectric properties.

Bismuth ferrite, BiFeO_3 , is one of the leading candidate materials for ferroelectric memory and electronic device applications. It has two important physical aspects, ferroelectric (Curie temperature = 1100 K) and magnetic (Néel temperature = 643 K) properties, simultaneously. However, it has a few draw-backs, such as high leakage current, which can be attributed to the valence electron state transition (Fe^{3+} to Fe^{2+}) and oxygen vacancies in the crystal structure. To understand the effect of the valence

electron sites of Fe in the target to the electrical and physical properties of the deposited BFO thin film, samples have been prepared with different iron valence states (Fe_2O_3 or Fe_3O_4) as starting materials.

1.2 Ferromagnetism

The ferromagnetic materials include transition (Ni, Co, Fe) and rare-earth (Sm, Nd) metal elements. The transition elements contain unpaired electrons with the appropriate interatomic distance and d orbital radius giving rise to a positive exchange integral for parallel spin alignment. The origin of the ferromagnetism can be described either based on the tight-band model or the itinerant model. [4] The tight-band model uses the concept of individual magnetic spin moments. The itinerant model is based on the fact that in the transition metals, the electron configuration forms a band structure. Figure 1.4 shows the typical electron band structure of a transition metal. For ferromagnetic materials the existence of a strong exchange field will cause the 3d electron energy band to split into different spin-up and spin-down electron densities. Therefore, the total spin-up and spin-down imbalance will result in a non-zero magnetization.

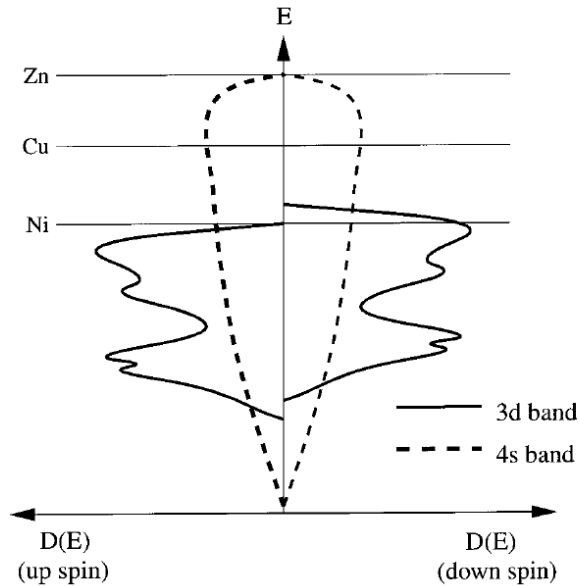


Figure 1.4 3d and 4s up- and down-spin densities of states in first-row transition metals, with exchange interaction included. [4]

Magnetic field dependence of ferromagnetic (ferrimagnetic) materials show hysteresis (figure 1.5). For a typical ferromagnet, starting from the demagnetized state ($H=M=0$), the magnetization increases with applied field following the OABC non-linear trace and reaches saturation state (M_s). Along the curve OABC, which is called virgin curve, a small initial part OA is reversible, where the magnetization can return to zero when the external field is removed. Beyond point A, the magnetization change becomes irreversible. When external field changes between positive and negative saturation fields, ferromagnetic magnetization will show the hysteresis loop as-shown CDEFGHC. For a typical hysteresis loop, magnetization is normally non-zero at $H=0$ (D, G), the magnitude of the magnetization at zero field is called remanent magnetization (M_r). The value of the field at which the magnetization equals to zero is called coercive field (H_c), which is also the half-width of the hysteresis loop.

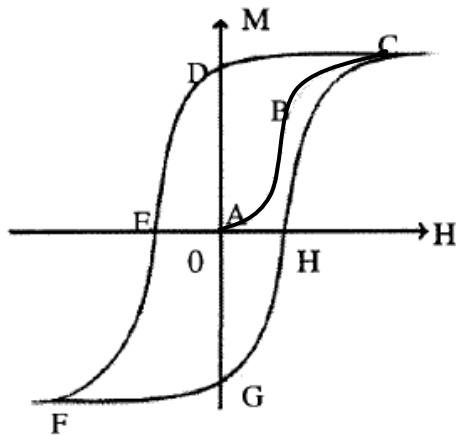


Figure 1.5 Magnetization-magnetic field hysteresis loops

Ferromagnetism comes from the electron-electron interaction, which is temperature dependent. The saturation magnetization of a magnetic material depends on temperature. With the saturation magnetization of a ferromagnetic material at absolute zero degree defined as M_0 , the saturated magnetization at an elevated temperature M will decrease. Figure 1.6 shows the schematic of the temperature dependence of a normalized saturation magnetization. A temperature increase causes thermal energy to increase and reduces the ferromagnetic ordering as the atoms lose the ordered magnetic moments which is related to a decreasing exchange interaction. The temperature at which a material loses ferromagnetism is called the Curie temperature Θ , above which the thermal fluctuation is strong enough to destroy the ferromagnetic ordering and the material transforms into a paramagnetic state.

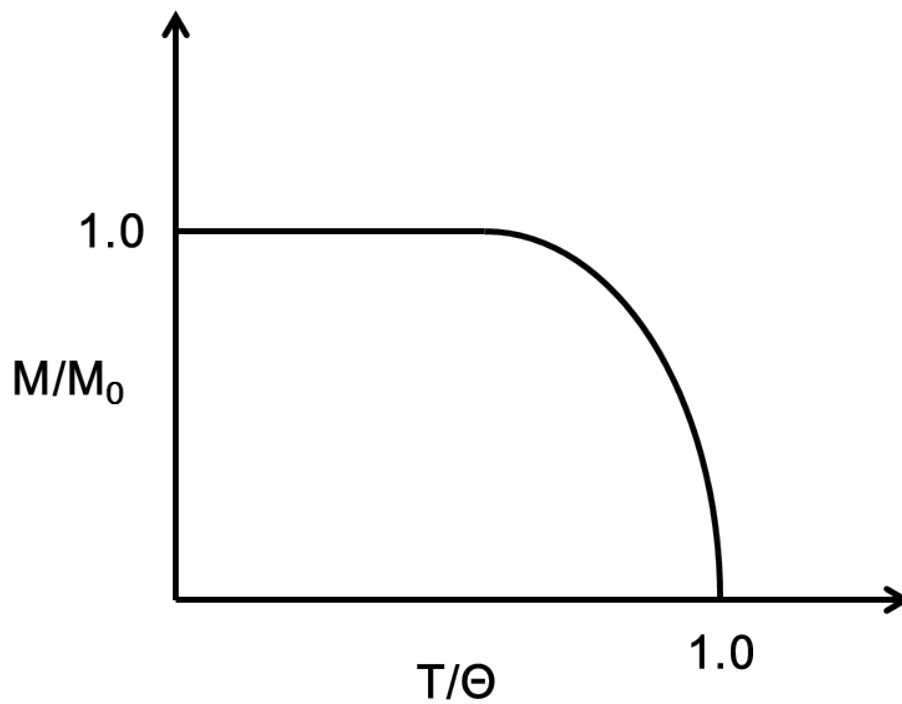


Figure 1.6 Typical temperature dependence of magnetization curves (Θ =Curie temperature, M_0 =saturated magnetization)

1.3 Antiferromagnetism

In typical antiferromagnetic materials, neighboring moments are aligned anti-parallel with a two dimensional representation of the magnetic moment configuration in the absence of external field shown in figure 1.7 (a). In an applied field, two types of magnetization responses can be identified (figure 1.7 (b)).

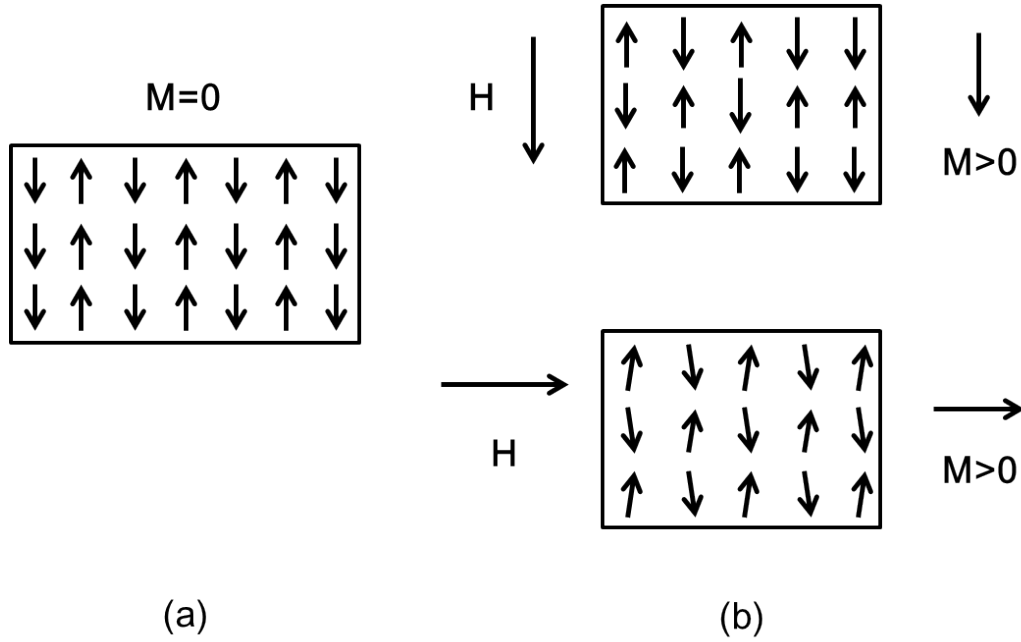


Figure 1.7 (a) Magnetic moment arrangement and (b) two magnetization response depend on external magnetic field of antiferromagnetic materials

If the applied field is parallel to the original spin direction, the magnetization resulting from the moments with the same direction as the applied field will exceed the magnetization from those with opposite magnetic moment direction. This will result in a positive susceptibility that can be calculated based on Weiss law . According to this theory, for two oppositely oriented spin sublattices of A and B, their interaction can be described by a molecular field

$$M_{A,B} = \frac{NM}{2} L \left(\frac{M(w_1 - w_2)M_{A,B}}{kT} \right) \quad (1.1)$$

Where w_1 is the interaction factor between the same spin directions, w_2 is the factor for the spin interaction between opposite spins, and L is the Langevin function. The solutions for Langevin function and molecular field indicate that the magnetic moments on the sublattices both decrease with increasing temperature. A critical temperature at

which the magnetic moments reach zero and beyond which the antiferromagnetic material loses its anti-parallel ordering is defined as the Néel temperature and can be defined as

$$\theta_N = \frac{NM^2(w_1 - w_2)}{6k} \quad (1.2)$$

If the applied field is perpendicular to the spin directions, the spin will rotate towards the field direction to minimize the Zeeman energy, which will result in a positive susceptibility. [5] This perpendicular susceptibility usually has a larger magnitude in comparison with the parallel counterpart and shows very weak temperature dependence. Figure 1.8 shows temperature dependence of the susceptibility for a single crystalline antiferromagnet with parallel and perpendicular applied fields and of a polycrystalline antiferromagnetic sample. For polycrystalline material, the magnetic moments have random distribution, so the total susceptibility is the average of the susceptibility along all direction.

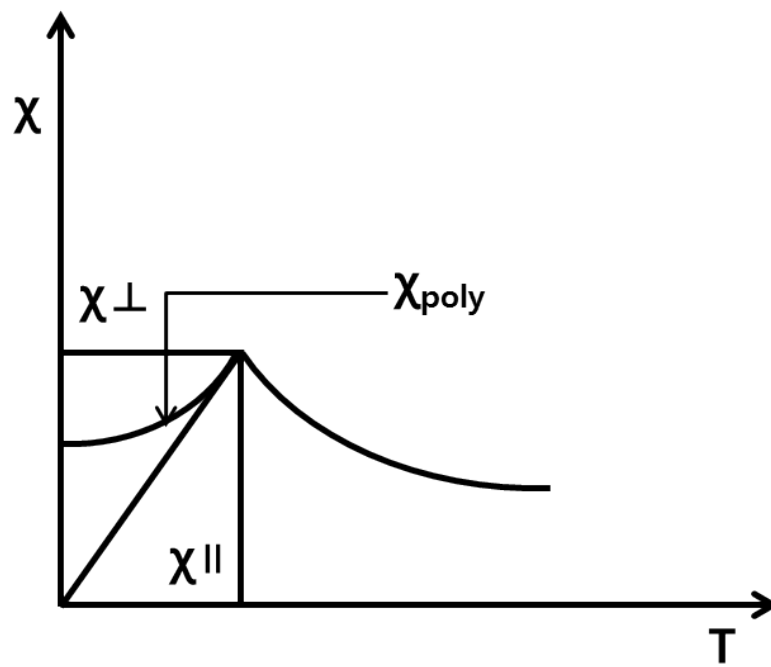


Figure 1.8 Temperature dependence of susceptibility for antiferromagnetic materials

(χ_{\perp} =perpendicular to the magnetic field, χ_{\parallel} =parallel to the magnetic field, and χ

poly=polycrystalline sample to the magnetic field).

1.4 Exchange Bias

The exchange bias effect is observed due to exchange coupling between magnetic moments of antiferromagnet (AFM) and ferromagnet (FM) layers at an interface. Exchange bias can be measured by field-cooling through the Néel temperature (T_N) of the AFM under a magnetic field (with the Curie temperature, T_C of the FM larger than T_N). [5,6] It can increase the coercive field or shift the hysteresis loop due to the exchange anisotropy. The first observation of exchange bias was shown using fine Co particles embedded in their native antiferromagnetic oxide (CoO). [6] Since then it has been observed in many different structures such as nanoparticle, nanowire, and thin films. Most of the recent studied on exchange bias mechanism have been performed on thin film systems. Nevertheless, thin films have potential industrial application because it allows a good control over the growth of the ferromagnetic and antiferromagnetic layers. The exchange bias effect is highly important in several important magnetic application such as high-density magnetic recording media and giant magnetoresistance effect (GMR). The value of the EB is affected by the roughness of the interface and defect formation in the Co/CoO. [7] These factors change the unidirectional exchange energy direction, which could be the reason for the asymmetric hysteresis loop.

Unidirectional anisotropy and exchange bias can be understood by assuming an exchange interaction at the antiferromagnet-ferromagnet interface from the structure. [6] When an external field is applied in the temperature range $T_N < T < T_C$, the FM spins are aligned with field, while the AFM spins remain randomly distributed (figure 1.9 (i)). When the temperature is cooled to $T < T_N$, the presence of the AFM spins near to the FM align ferromagnetically to those of the FM layer. The other spins in the AFM follow the AFM order so as to produce zero net magnetization (figure 1.9 (ii)). When the magnetic field is

reversed, the FM spins start to rotate. However the AFM spins remain unchanged from the sufficiently large AFM anisotropy (figure 1.9 (iii)). Therefore, the interfacial interaction between the FM-AFM spins at the interface exert a microscopic torque on the ferromagnet spins, to keep them in their original position (ferromagnetically aligned at the interface) (figure 1.9 (iv)). The FM spins have one single stable configuration, i.e. the anisotropy is unidirectional. Thus, the field needed to completely reverse the FM layer will be larger if it is in contact with an AFM layer, because an extra field is required to overcome the microscopic torque. However, once the field is rotated back to its original direction, the FM spins will start to rotate at a smaller field, due to the interaction with the AFM spins (which exert a torque in the same direction as the field) (figure 1.9 (v)). The material behaves as if there was an extra (internal) biasing field, the FM hysteresis loop is shifted in the field axis.

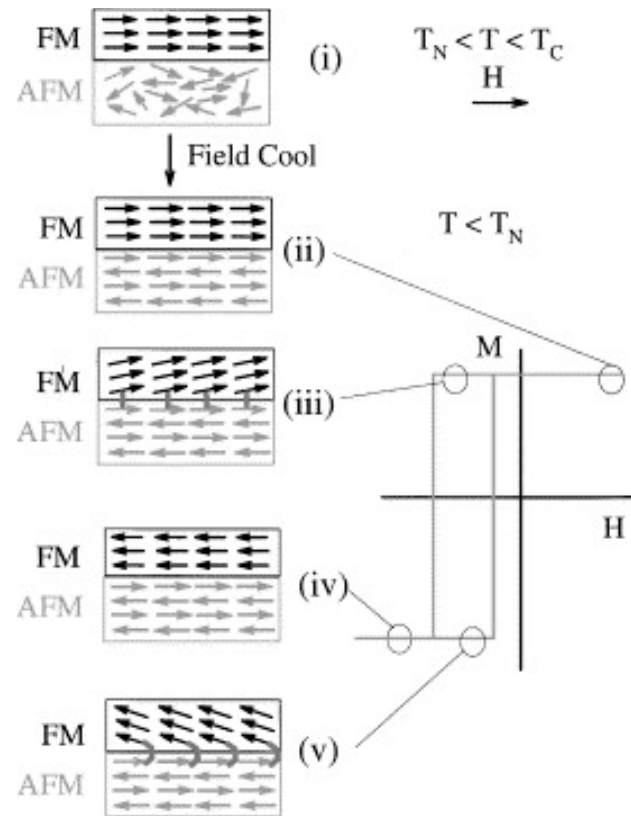


Figure 1.9 Field dependence spin orientation behavior of magnetic hysteresis loop. (i), (ii) saturated point at positive field, (iii) positive to negative field point, (iv) saturated point at negative field, (v) minimized negative field. [6]

Chapter 2

Sample Preparation Methods and Experimental Techniques

2.1 Sample Preparation Methods

2.1.1 Sputtering Method

Sputter deposition method is one of the physical vapor deposition methods for thin film fabrication. Sputtering involves ejecting atoms from a raw material (target) onto a substrate (single crystal or polycrystalline). Re-sputtering is re-emission from the deposited material during the deposition process by ion or atom bombardment. The sputtered ions, typically only a small fraction of the ejected particles (1%) are ionized, can fly from the target in straight lines and impact energetically on the substrates or vacuum chamber causing re-sputtering.

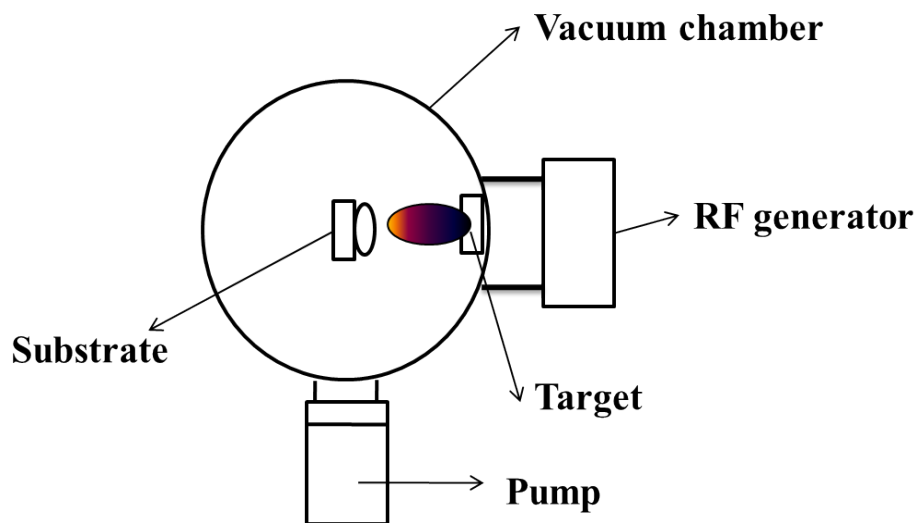


Figure 2.1 Schematic of RF sputtering methods.

Sputtered atoms ejected from the target have a wide energy distribution with glow shape. The glow shape is changed with argon pressure and source power. Film

thickness is developed with deposition time and distance from target to substrate. Also, the angle between target and substrate could affect growth direction of the thin film.

Followings are a typical procedure of sputtering method.

1. Substrate is ultrasonic cleaning in the acetone.
2. Blowing by nitrogen gas to substrate to remove the acetone.
3. Holding the substrate on the substrate holder.
4. Running the sputtering machine with rotary pump to make a vacuum state lower than 10^{-2} Torr.
5. Running the turbo molecular pump to make a vacuum state lower than 10^{-6} Torr.
6. Pre-deposition of the target to remove the surface dust.
7. Depositioning the target material on substrate.
8. Turn off the turbo molecular pump after deposition.
9. Venting the chamber with nitrogen gas.

2.1.2 Pulsed Laser Deposition Method

Pulse laser deposition (PLD) is one of the physical vapor deposition methods. In 1980, high temperature superconductor thin films were studied by pulsed laser deposition. Afterwards, the technology was widely adapted for ferroelectric, ferromagnetic, and giant magnetoresistance thin film areas, because of its advantage on complex oxides film deposition.

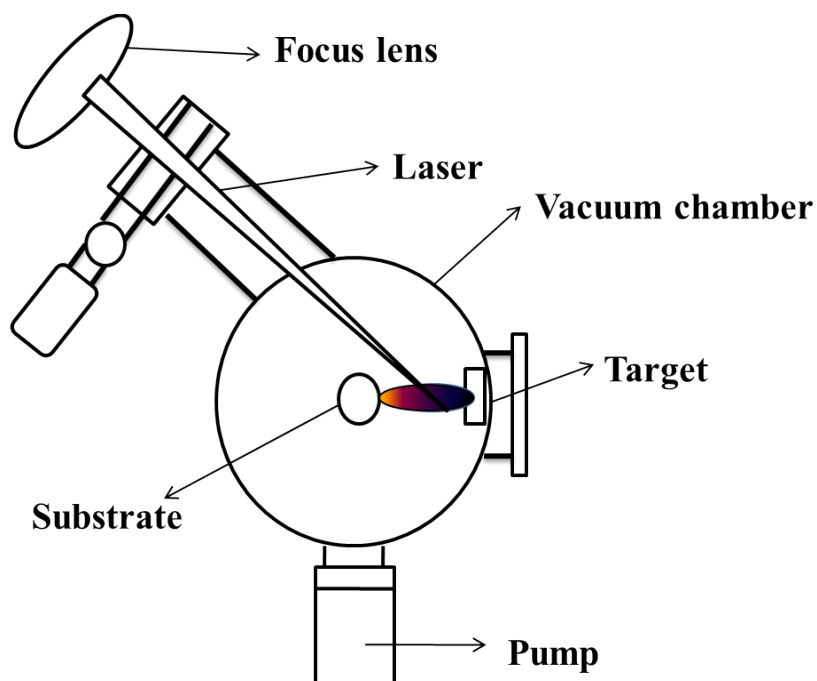


Figure 2.2 Schematic of PLD methods.

Figure 2.2 Shows the schematic diagram of PLD system.

Incoming pulsed laser generated by a Kr:Fgas laser focused onto the target materials to evaporate atoms as plasma states. The evaporated atoms were transferred onto the substrates and the arrived atoms will find energetically favorable site on the substrate to crystallize. During deposition, oxygen pressure in the deposition chamber was controlled to optimize film growth condition.

Super-heating is the mechanism for PLD system. In the thermal evaporation method, the composition of the vapor depends on the elemental vapor pressures of the target resulting in compositional differences between vapor and target. However, laser-induced expulsion produces a plume of material with a stoichiometry similar to that of the target. It is generally easier to obtain the desired film stoichiometry for multi-element materials using PLD than with other deposition technologies.

Followings are a typical procedure of film deposition by a PLD method.

1. Cleaning substrate by acetone in an ultrasonic agitator.
2. Blowing nitrogen gas to the substrate to remove the acetone.
3. Attaching the substrate on the substrate holder as a heater.
4. Turning on the rotary pump to make a vacuum state lower than 10^{-2} Torr.
5. Turning on the turbo molecular pump to make a vacuum state lower than 10^{-6} Torr.
6. Pre-running the pulsed excimer laser to make a stabilization of the laser power.
7. Pre-ablation of the target material to make a stabilization of the plume.
8. Depositioning of the target material onto substrate.
9. Turn off the laser and turbo molecular pump after deposition,.
10. Venting the chamber with nitrogen gas.

2.2 Characterization Methods

2.2.1 X-ray Diffraction (XRD)

X-ray Diffraction (XRD) allows the study of the formation of phases within thin films on a substrate. The X-rays were generated from a Cu target with a wavelength of $K_1\alpha = 1.540562 \text{ \AA}$ and $K_2\alpha = 1.544398 \text{ \AA}$. Diffraction patterns were measured in a θ - 2θ scan mode. The incident x-ray angle was rotated with an θ angle and the detector rotation angle with a 2θ angle. The X-ray diffractometer was operated at an accelerating voltage of 30 kV and current of 15 mA.

2.2.2 Scanning Electron Microscopy (SEM)

Scanning Electron Microscopy was used for investigating morphologies of films and thicknesses of thin films. Samples are cut in half after deposition and the fresh cross section was used for cross sectional SEM images.

2.2.3 X-ray Photoelectron Spectroscopy (XPS)

XPS was used for measuring chemical binding energy states at the surface of the thin films. XPS is a surface-sensitive quantitative spectroscopic technique that measures the elemental composition at a parts per thousand range, empirical formula, chemical state and electronic state of the elements that exist within a few layers of surface of material. XPS spectra are obtained by irradiating a material with a beam of X-rays while simultaneously measuring the kinetic energy and number of electrons that escape from the top 0 to 10 nm of the material being analyzed. XPS requires high vacuum or ultra-high vacuum conditions, although a current area of development is ambient-pressure XPS, in which samples are analyzed at pressures of a few tens of millibar. The peaks were studied with an XPS analysis program of XPSPEAK 4.1.

2.2.4 P-E Loop

Ferroelectric properties of the Polarization-Electric field hysteresis loops were measured by a Sawyer-Tower circuit with an oscilloscope and a function generator. Ferroelectric hysteresis loops were measured at 10 kHz of AC frequency at room temperature.

2.2.5 M-H Loop

Ferromagnetic hysteresis loop of exchange bias behaviors was measured after field cooling with 5000 Oe from room temperature to 10 K.

2.2.6 Leakage Current Density

Leakage current density was measured by a current-voltage curve. It is measured at room temperature with DC bias voltage. The mechanism of leakage current behavior is studied with space-charge limited conduction and interface limited Fowler-Nordheim tunneling.

Chapter 3

Ferroelectric and Ferromagnetic Behavior of BiFeO₃ Thin Films with Different Iron Valence Electron State

The bismuth ferrite, BiFeO₃, is one of the candidate materials for multiferroic memory and electronic device applications. It has two important physical aspects, ferroelectric and magnetic properties. [8] Based on first principle calculations, the electron orbital hybridization between Bi(6s,6p) and O(2p) leads to ferroelectric polarization behavior. Also Fe(3d) and O(2p) in the valence band leads to antiferromagnetic spin moment. [9-11] However, it has a few drawbacks for ferroelectric application, such as high leakage current, which may be allocated to the valence electron state of iron (Fe^{2+}) and oxygen vacancies in the structure (Vos). [12,13] On the other hand, the valence electron state of iron (Fe^{2+}) may increase the magnetic moment due to the increasing canted angle between interacting Fe ions. [14,15]

In this chapter, Polycrystalline BFO films are fabricated by PLD method from two different starting raw material powders (Fe_2O_3 or Fe_3O_4) with Bi_2O_3 powder. The electrical and magnetic properties are studied with valence electron state of iron and oxygen states.

3.1 Sample Preparation of BiFeO₃ Thin Films

Both BFO(Fe_2O_3) and BFO(Fe_3O_4) targets were prepared by a conventional solid solution reaction method. Bi_2O_3 (Aldrich, 99.9%) were mixed with Fe_2O_3 (Aldrich, 99%) (here after BFO(Fe_2O_3)) or Fe_3O_4 (Aldrich, 98%) (here after BFO(Fe_3O_4)) powders at calculated mol weight. Mixed powders were ball-milled with alcohol and calcinated at 700 °C. After calcinations, powders were pressed into disks and sintered at 820 °C.

Polycrystalline BFO(Fe_2O_3) and BFO(Fe_3O_4) thin films were fabricated on Pt/Ti/SiO₂/Si substrates using a pulsed laser deposition technique employing a Kr:F excimer laser with a wavelength of 248 nm. Thin films were grown at an optimized condition; deposition

temperature of 530 °C, oxygen pressure of 30 mTorr, and laser repetition frequency of 5 Hz. The thicknesses of BFO(Fe_2O_3) and BFO(Fe_3O_4) films were approximately 700 nm observed by scanning electron microscopy.

3.2 Analysis of BiFeO₃ Thin Films

3.2.1 X-ray Diffraction Analysis

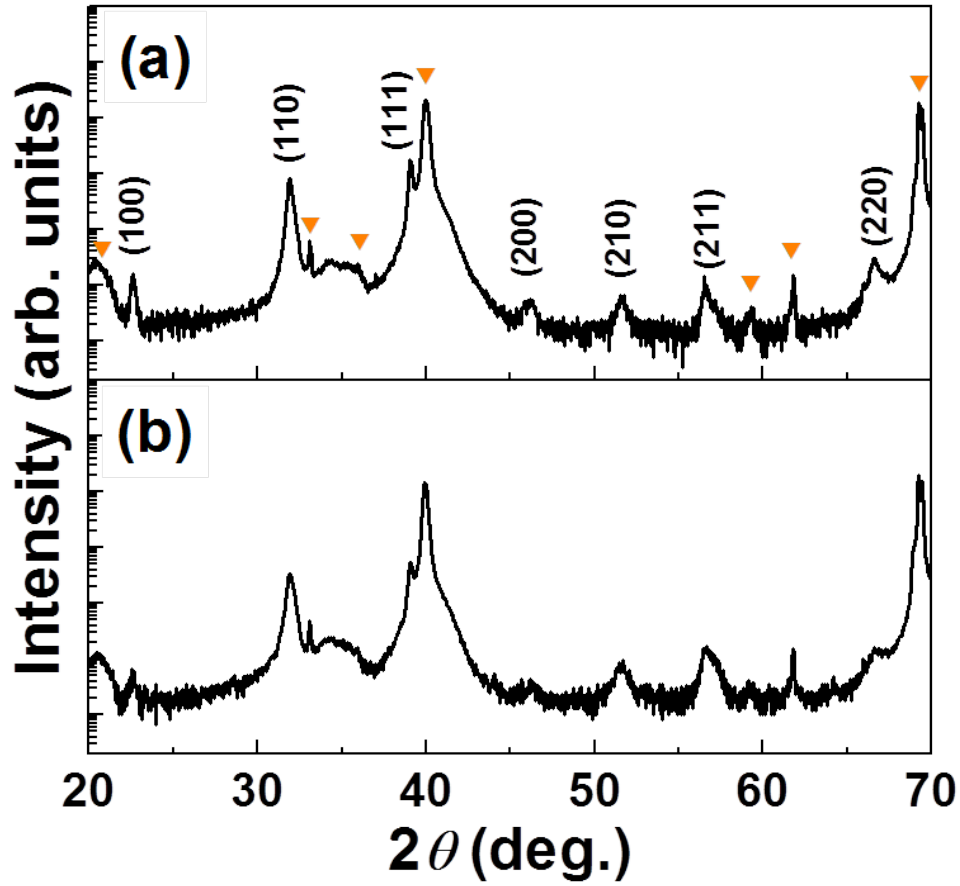


Figure 3.1 X-ray diffraction patterns of (a) BFO(Fe_2O_3) and (b) BFO(Fe_3O_4) thin films.

(∇ : substrate peaks)

X-ray diffraction (XRD) patterns of BFO(Fe_2O_3) and BFO(Fe_3O_4) thin films were shown in figure 3.1. Both films were identified as a rhombohedrally distorted perovskite

structure (R3m) without any preferential orientation. [16] Based on the measured XRD, any detectable secondary phases were not observed within the sensitivity of the x-ray diffractometer. Therefore, it is reasonable to assume that the measured electrical and magnetic properties of the films come from the main BFO structures not from any secondary phases in the films.

3.2.2 SEM Analysis

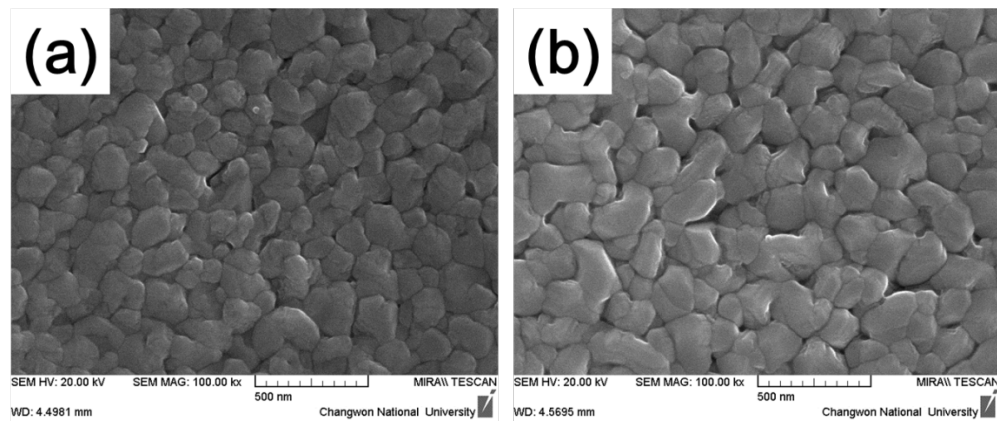


Figure 3.2 FE-SEM images of surface from (a) BFO(Fe_2O_3) and (b) BFO(Fe_3O_4)

Surface morphologies of BFO(Fe_2O_3) and BFO(Fe_3O_4) films observed by SEM are shown in figure 3.2. Both films exhibit a similar morphology and a similar grain size, even though both films were deposited from different targets with different starting Fe valence states.

3.2.3 X-ray Photoelectron Spectroscopy Analysis

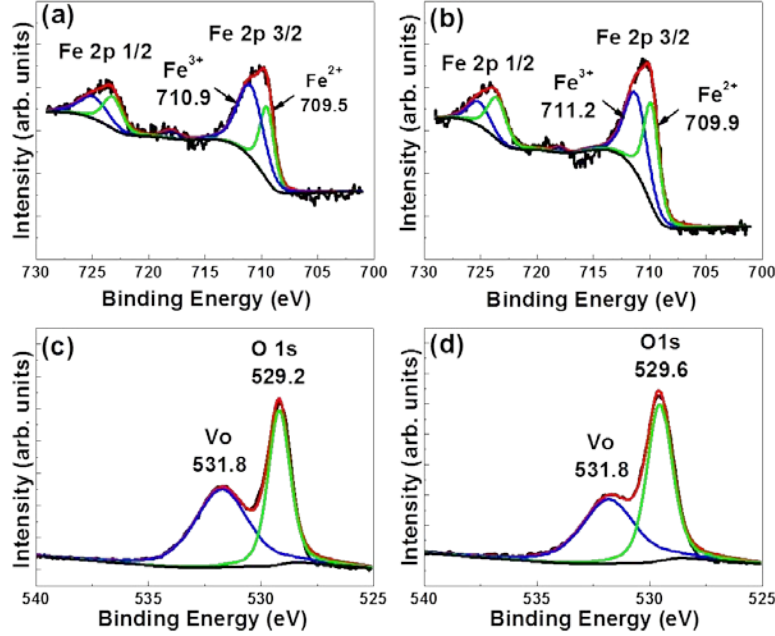


Figure 3.3 XPS spectra of (a) BFO(Fe_2O_3), (b) BFO(Fe_3O_4) in Fe site and (c) BFO(Fe_2O_3), (d) BFO(Fe_3O_4) in O site.

An ideal BFO should have only Fe^{3+} to satisfy charge neutrality. However, BFO thin films could contain Fe^{2+} electron state to make a new charge neutral state invoked by oxygen vacancies. Valence electron states of both BFO films were investigated by x-ray photoelectron spectroscopy (XPS). The binding energy spectra for Fe 2p signal measured from BFO(Fe_2O_3) and BFO(Fe_3O_4) thin films are shown in figure 3.3 (a) and (b), respectively. Peak positions of Fe 2p 1/2 and Fe 2p 3/2 orbital spectra were confirmed by the XPSPEAK 4.1 fitting program. Each Fe 2p peak can be further deconvoluted into two separate peaks depending on the valence electron states of Fe, such as Fe^{3+} and Fe^{2+} .

The peak positions of the Fe 2p 3/2 have been reported to be 711.0 eV for Fe^{3+} and 709.5 eV for Fe^{2+} . [15,17] As shown in figure 3.3, these were estimated as 710.9 eV

(Fe^{3+}) and 709.5 eV (Fe^{2+}) for the $\text{BFO}(\text{Fe}_2\text{O}_3)$ thin film, and 711.2 eV (Fe^{3+}) and 709.9 eV (Fe^{2+}) for the $\text{BFO}(\text{Fe}_3\text{O}_4)$ thin film. The peak positions of Fe in $\text{BFO}(\text{Fe}_3\text{O}_4)$ thin film were shifted to slightly higher binding energy than those of the $\text{BFO}(\text{Fe}_2\text{O}_3)$ thin film. It has been reported that the XPS peak shift to higher binding energy was related to the cation substitution effects in Bi and/or Fe sites. [18-21] The Fe^{3+} to Fe^{2+} ratio were estimated to be 64:36 in the $\text{BFO}(\text{Fe}_2\text{O}_3)$ and 52:48 in the $\text{BFO}(\text{Fe}_3\text{O}_4)$ thin films from the fitted areas of the deconvoluted curves. This result suggest that the ionic states of Fe in the films were changed from Fe^{3+} to Fe^{2+} which may be induced from oxygen deficiency at the surface of the films.

The XPS spectra of oxygen in the surface of $\text{BFO}(\text{Fe}_2\text{O}_3)$ and the $\text{BFO}(\text{Fe}_3\text{O}_4)$ thin films were shown in figure 3.3 (c) and (d). The O1s peak positions are 529.2 eV in the $\text{BFO}(\text{Fe}_2\text{O}_3)$ and 529.6 eV in the $\text{BFO}(\text{Fe}_3\text{O}_4)$. Oxygen vacancy related peaks appeared at the binding energy of 531.8 eV.¹⁷ The O1s to Vos ratio were estimated to be 55:45 in the $\text{BFO}(\text{Fe}_2\text{O}_3)$ and 64:36 in the $\text{BFO}(\text{Fe}_3\text{O}_4)$ thin films from the fitted areas of the deconvoluted curves. By comparing the area of the oxygen vacancy related curves, the number of oxygen vacancy in $\text{BFO}(\text{Fe}_2\text{O}_3)$ film is expected to be larger than that in $\text{BFO}(\text{Fe}_3\text{O}_4)$ thin film.

3.2.4 P-E Hysteresis Loop Analysis

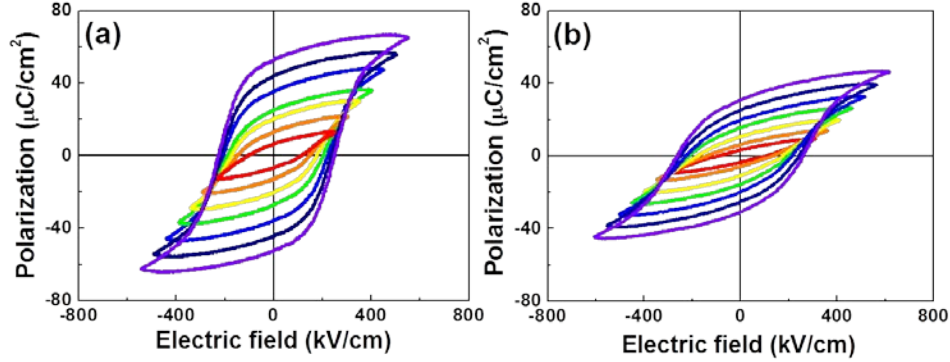


Figure 3.4 Ferroelectric hysteresis loops of (a) BFO(Fe_2O_3) and (b) BFO(Fe_3O_4) thin film measured with frequency at 10 kHz.

The ferroelectric hysteresis loops of BFO(Fe_2O_3) and BFO(Fe_3O_4) thin films were measured at room temperature with 10 kHz of switching frequency as shown in figure 3.4 (a) and (b). Remanent polarization ($2P_r$) of BFO(Fe_2O_3) film ($106 \mu\text{C}/\text{cm}^2$) is twice as large as that of the BFO(Fe_3O_4) film ($51 \mu\text{C}/\text{cm}^2$) at the same electric field of 600 kV/cm, while both films exhibit a similar coercive electric fields ($2E_c$) of 454 and 496 kV/cm, respectively. The observed difference in the remnant polarization from two films might be related with the difference in the valence electron states observed from XPS measurements as shown in figure 3.3. Since remnant polarization should be strongly related with the FeO_6 octahedron in BFO, contribution from the FeO_6 octahedral in a given volume could exhibit larger remnant polarization at the surface. [20,21] If BFO has a FeO_6 octahedral state with less charged Fe, such as Fe^{2+} rather than fully charged Fe^{3+} , polarization from the octahedral could be reduced resulting in less polarization. The BFO(Fe_3O_4) thin film exhibit a larger number of Fe^{2+} states than that of the BFO(Fe_2O_3) thin film from the surface, which may suggest that a smaller remnant polarization could be expected from the BFO(Fe_3O_4) thin film. Therefore, it could be concluded that the

charge neutrality of BFO and stable state of the octahedral FeO_6 are an important factor for a ferroelectric property.

3.2.5 Leakage Current Density Analysis

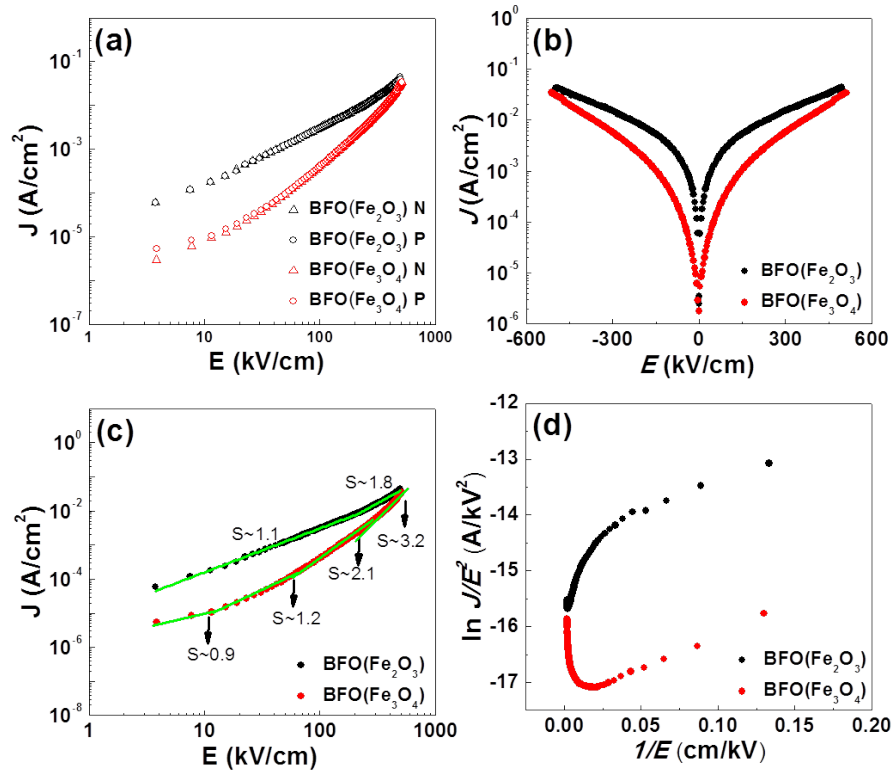


Figure 3.5 Leakage current density (J) versus electric field (E) of BFO(Fe_2O_3) (black) and BFO(Fe_3O_4) (red) plot in (a) symmetry of negative and positive bias, (b) $\log(J)$ vs linear (E) (c) $\log(J)$ vs $\log(E)$, and $\ln(J/E^2)$ vs $1/E$.

Applied DC electric field dependent current behaviors of BFO(Fe_2O_3) and BFO(Fe_3O_4) thin films are shown in figure 3.4 (a). Both BFO(Fe_2O_3) and BFO(Fe_3O_4) thin films exhibited symmetrical current behaviors at positive (P) and negative (N) bias field. However, BFO(Fe_2O_3) and BFO(Fe_3O_4) thin films exhibited different conduction behaviors as shown in figure 3.5 (b). In low electric field, BFO(Fe_2O_3) film exhibited lower

resistivity than BFO(Fe_3O_4) film. This could be attributed to the large number of oxygen vacancies in BFO(Fe_2O_3) film as shown in figure 3.3. The oxygen vacancy may act as a charged carrier in the BFO when a weak electric field was applied. On the other hand, under high electric field, leakage current densities of both BFO(Fe_2O_3) and BFO(Fe_3O_4) films became equal. Therefore, it needs to be further investigated for understanding why conducting behaviors were changed when the electric field was increased.

It has been known that there are two different leakage current mechanisms in ferroelectric thin films; a space charge limited conduction (SCLC) and an interface limited Fowler-Nordheim (FN) tunneling. Both mechanisms were plotted in figure 3.5 (c) and (d), respectively. According to Lampert's [22-25] theory of the SCLC mechanism, ohmic conduction behavior ($J \propto E^\alpha : \alpha \sim 1$), modified Child's law conduction ($J \propto E^\alpha : \alpha \sim 2$), and trap filled limit behavior ($J \propto E^\alpha : \alpha > 2$) are defined by the transition voltage V_c (Ohmic to modified Child's law) and V_{TFL} (modified Child's law to Trap-Filled-Limit) are described by the following equation,

$$V_c = \frac{ed^2}{2\varepsilon_0\varepsilon_r\theta}, \quad (3.1)$$

$$V_{TFL} = \frac{eN_t d^2}{2\varepsilon_0\varepsilon_r}, \quad (3.2)$$

where ε_r and ε_0 are dielectric constant of material and dielectric permittivity of vacuum, d is thickness of the film, N_t is the total trap density, and θ represents the ratio of the free carrier density to the density of the filled trapping sites given by

$$\theta = \frac{N_c}{N_t} \exp\left(\frac{-E_t}{k_B T}\right), \quad (3.3)$$

where N_c is the effective density of states in the conduction band, E_t is the energy level of carrier trap sites, and $k_B T$ is the thermal energy. Then, the leakage current for modified Child's law conduction is determined as

$$J_{SCLC} = \frac{9\mu\epsilon_r\epsilon_0}{8d} E^2, \quad (3.4)$$

where E is the applied electric field and μ is the carrier mobility.

The $\log J$ vs $\log E$ graph represents the SCLC mechanism as shown in figure 3.2.

(c). The V_c of BFO(Fe_2O_3) is 200 kV/cm, on the other hand, the V_c of BFO(Fe_3O_4) film is 80 kV/cm and V_{TFL} is 200 kV/cm. It has been known that the FN tunneling was a kind of charge carrier tunneling from electrode through an interfacial energy into a ferroelectric layer. [25-27] It could be expressed as following,

$$J_{FN} = BE^2 \exp\left(\frac{-C\phi_i^{2/3}}{E}\right) \quad (3.5)$$

where B and C are constants and ϕ_i is a potential barrier height. If the FN tunneling was dominant in leakage current, the slope α in $\ln(J/E^2) - (1/E)$ plot should increase sharply at a high electric field and slope α can be used to calculate the potential barrier height $\phi_i = (\alpha/C)^{2/3}$. The FN tunneling was observed in figure 3.4 (d). The BFO(Fe_3O_4) film exhibits FN tunneling above 200 kV/cm. On the other hand, the BFO(Fe_2O_3) film does not exhibit the FN tunneling. As previously reported, Qi *et al.* demonstrated that the SCLC mechanism originated from shallow-level traps in the band gap which could be induced by oxygen vacancies. [28] Also Yang *et al.*, reported that Fe^{2+} ions mainly affected on FN tunneling at high electric field in BFO film. [29] The observed leakage current behaviors and XPS results from both films match well; the BFO(Fe_2O_3) film with only SCLC mechanism exhibited larger number of oxygen vacancies and lower concentration of Fe^{2+} ions than those of the BFO(Fe_3O_4) film with both SCLC and FN tunneling mechanisms.

3.2.6 M-H Hysteresis Loop

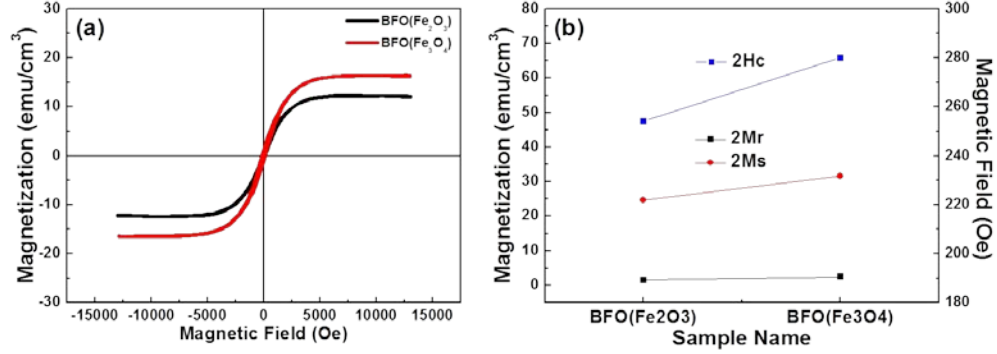


Figure 3.6 Magnetic hysteresis loops of (a) BFO(Fe₂O₃) and BFO(Fe₃O₄) thin film (b) collected data from (a).

Figure 3.6 (a) is shown the magnetic hysteresis loop measurement result.

Magnetic hysteresis loops are measured with applied magnetic field at 14000 Oe at room temperature. Magnetization is calculated with sample volumes. From the measurement result, saturated and remanent magnetization of BFO(Fe₃O₄) is higher than BFO(Fe₂O₃). Also, the coercive field of BFO(Fe₃O₄) is higher than BFO(Fe₂O₃). From the XPS results, BFO(Fe₃O₄) has more Fe²⁺ volume ratio than BFO(Fe₂O₃). It means that the magnetic behavior of BFO(Fe₃O₄) is affected by Fe²⁺. The Fe²⁺ state is introduced which breaks the spin symmetry. [11] It will also tilt to increasing the angle between two different irons.

3.3. Conclusion

Polycrystalline BFO(Fe_2O_3) and BFO(Fe_3O_4) films were fabricated on Pt/Ti/SiO₂/Si substrates. The BFO(Fe_2O_3) and BFO(Fe_3O_4) films exhibit different PE hysteresis behaviors. The BFO(Fe_3O_4) was dominated by charged defect distribution with Fe^{2+} ions at the surface. remnant polarization of the BFO(Fe_2O_3) was two times larger than that of the BFO(Fe_3O_4) film, which may be related to the structural stability through the relatively better charge neutrality of FeO_6 octahedral in the BFO(Fe_2O_3) film. The leakage current behaviors of both films were found to be different due to the different concentrations of Fe^{2+} and oxygen vacancies at the surface. The conduction mechanisms of BFO(Fe_3O_4) film was agree well to the SCLC and the FN tunneling mechanisms by coexistence of relatively high concentrations of both Fe^{2+} ions and oxygen vacancies, while that of BFO(Fe_2O_3) film was dominated by the SCLC mechanism from the high concentration of oxygen vacancies and relatively low concentration of Fe^{2+} ions. The BFO(Fe_2O_3) and BFO(Fe_3O_4) films exhibit different magnetization hysteresis behaviors. Magnetic properties are related with Fe^{2+} ratio. BFO(Fe_3O_4) film is more tilted between iron atoms with higher Fe^{2+} valence electron state then BFO(Fe_2O_3).

Chapter 4

Exchange Bias Behavior of Co/CoO Bilayer on Flat and Modulated Substrates

Exchange bias behavior is one of the important phenomena in magnetic materials. It was observed from cobalt particles with embedded oxygen in 1956. [31] After the observation, the exchange bias behavior has been studied for applications in giant magnetoresistance (GMR) and spin electronics.

In a ferromagnetic-antiferromagnetic system, the temperature region of the exchange-bias field is observed lower than the Néel temperature. For example, the exchange-bias field of Co/CoO bilayer thin film is observed lower than the Néel temperature of CoO (295 K). Exchange bias behavior of a Co/CoO bilayer is associated with a uniaxial direction of exchange anisotropy. [32,33]

This chapter describes the exchange bias behavior of Co/CoO bilayer on flat and modulated substrate system. For the flat substrate system, we prepared the Co/CoO samples on Si substrate. The exchange bias and the training effect behaviors are studied with magnetization hysteresis loop. For the modulated substrate system, we prepared the Co/CoO bilayer on modulated substrate. The modulated substrate surface is observed by SEM and TEM images. The exchange bias effect is studied with numerical calculation and measured hysteresis loops.

4.1 Sample Preparation of Co/CoO Thin Films

We have prepared two different substrates, one flat and one modulated. First of all, the flat substrate, we used commercial Si wafer. The Co layer was deposited on Si wafer by sputtering method. The condition of sputtering, Ar pressure and RF power are kept at 50 mTorr and 100 W. Thickness of Co layer is controlled with different deposition time. After preparation of the Co layer, it was exposed to air to form a CoO layer on top of the Co layer.

The modulated substrate is prepared by the following method. The modulated substrates were fabricated by electrodeposition of Au into self-assembled polystyrene microsphere crystal template. Co film was then DC sputter deposited onto both flat (Au coated Si wafer) and the modulated substrate. The chamber base pressure is 10^{-6} Torr. The argon pressure during deposition was 10 mTorr, and power was 100 W. After Co deposition, the oxygen was introduced into the chamber, and restarted the deposition for predetermined time.

Magnetization hysteresis loops were recorded at 10 K using a superconducting quantum interference device (SQUID) magnetometer. Before the measurements, the sample was cooled down from 300 K to 10 K under a magnetic field of 5000 Oe. Scanning electron microscopy SEM was carried out using a JEOL 6700 FE SEM.

4.2 Analysis of Co/CoO Thin Films

4.2.1 Exchange Bias Behavior of Co/CoO Bilayer on Flat Substrate

This part will be discussed for Co/CoO bilayer on flat substrate system. The exchange bias phenomena of this system shows exchange coupled Co and CoO layers. The training effect phenomenon of this system shows the domain-wall relaxation from first to second measurements.

4.2.1.1 M-H Hysteresis Loop Analysis

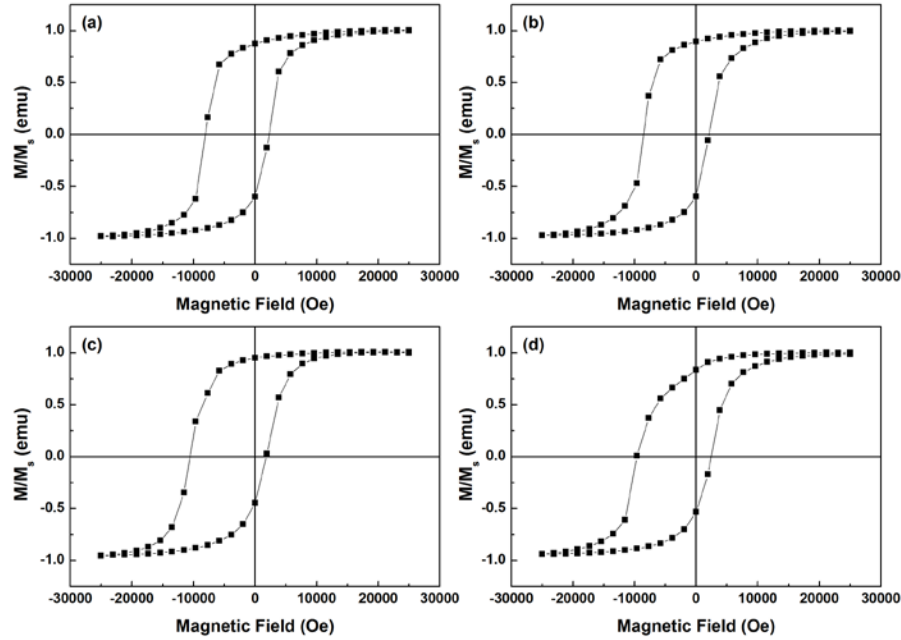


Figure 4.1 Magnetic hysteresis loops of Co/CoO bilayer on flat substrate with different Co thicknesses (a) Co=20 nm, (b) Co=12 nm (c) Co=9 nm and (d) Co=7 nm.

Magnetization reversal behavior is measured with different cobalt thicknesses after field-cooling process with 5000 Oe from 300 K to 10 K. The squareness of hysteresis loops is clearly shown from entire samples. Based on the observation, the Co/CoO bilayer thin films have unidirectional anisotropy axis. Because of the flat substrate, the interface of the Co/CoO bilayer takes the unidirectional anisotropy direction during the field-cooling process. This anisotropy causes the shift of the loop to negative field. It is called the negative exchange bias.

The negative exchange bias included the following physical properties: [6, 34, 35]

- (1) CoO layer has a strong anisotropy

(2) The spin moments at the Co/CoO interface is exchange coupled, allowing the Co moment to be pinned by the CoO anisotropy.

(3) The spins within the Co layer are exchange coupled.

(4) If an external field is applied to the samples at some angle relative to the pinning direction, the anisotropy axis of the CoO layer may be rotated away from the pinning direction by interaction with the Co layers.

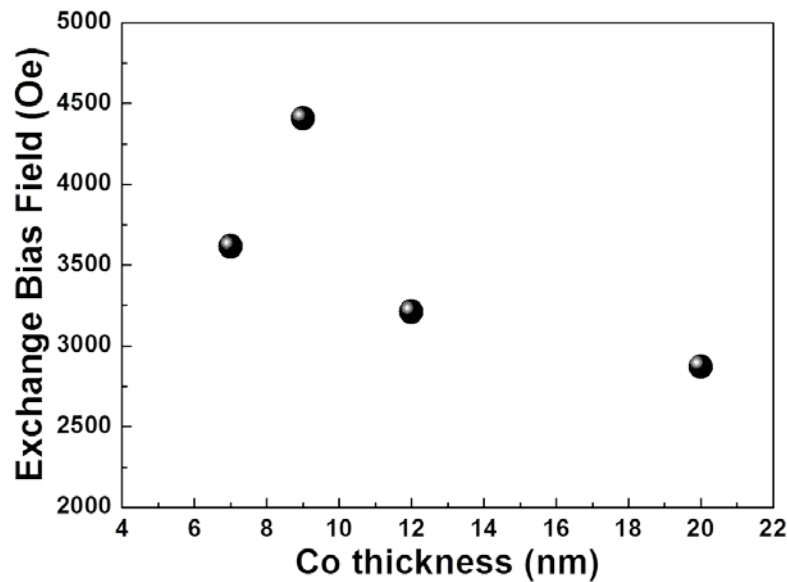


Figure 4.2 Co thickness versus exchange bias results.

The Co thickness dependence of the negative exchange bias field is shown in figure 4.2. It is seen that the exchange bias field gradually decreases except at 9 nm thickness sample. Generally, the exchange bias field increases with inverse Co thickness. [36] However, the interface of a Co/CoO bilayer is complicated due to the grain growth mode. If the thickness roughness is changed by complex grain growth mode, the exchange coupling is increased by the high roughness compared to similar thickness films. One other way to describe the exchange bias is that the CoO phase is

polycrystalline. Because the Co layer is exposed in the air, the CoO layer may have several phases like CoO, Co₂O₃ and Co₃O₄. The complex mixture cobalt oxides can lead to complicated exchange coupling at low temperatures.

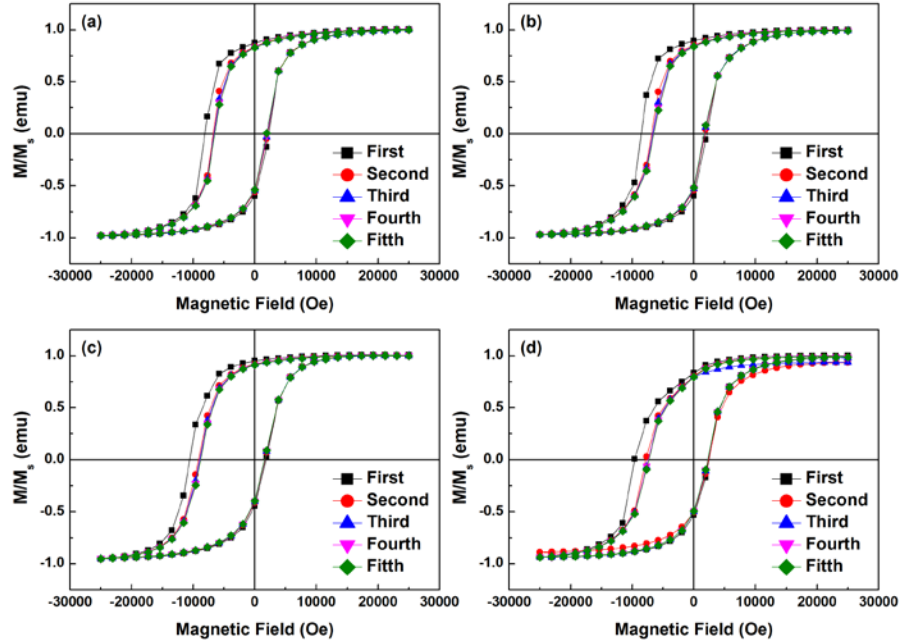


Figure 4.3 Training effects of Co/CoO bilayer on flat substrate (a) Co=20 nm, (b) Co=12 nm (c) Co=9 nm and (d) Co=7 nm.

The training effect from exchange bias is observed in the figure 4.3. The Co/CoO bilayer thin films are measured with the number of hysteresis loops cycled after preparation of the initial state of exchange bias via the field cooling procedure. The training effect is widely accepted with two explanations. One is an unstable state of the antiferromagnetic layer. The other is interface between the antiferromagnet and ferromagnet prepared by a field cooling procedure. [6, 37]

The training effect is clearly observed with five-cycled measurement. The remanent magnetization is decreased with increasing measurement cycles. It is related to partial loss of the magnetization in the CoO domains. Because of the unstable exchange coupling between Co and CoO layer, domain-wall motion is relaxed with measurement cycling. Also, The interface transition towards the equilibrium state is faster than the transition of the “frozen” spins towards their stable configuration.

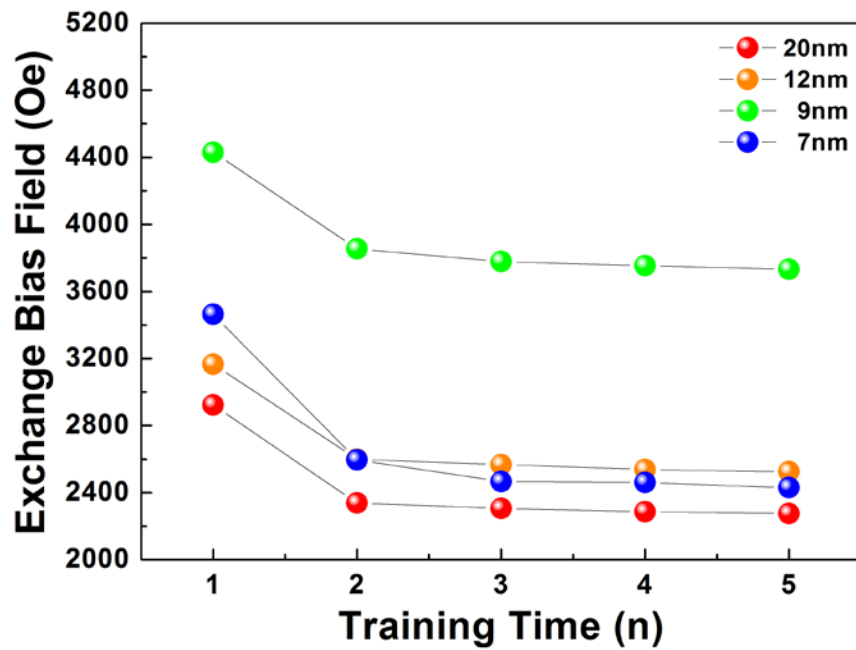


Figure 4.4 Training time versus exchange bias results.

The training effect result is summarized in figure 4.4. Exchange bias is decreases with increasing measurement time. The magnetization reversal behavior of Co/CoO bilayer is relaxed at first to second time. However, the slope of the figure 4.4 is linear dependent from the second to fifth measurement. It is related to the domain pinning region decreasing from first to second measurement. After second measurement, remained a domain pinning region is the frozen state during the cycling measurement.

4.2.2 Exchange Bias Behavior of Co/CoO Bilayer on Modulated Substrate

This part will be discussed for Co/CoO bilayer on modulated substrate system.

The exchange bias behavior of this system is shown with two-stage magnetization switching from M-H hysteresis loop. The two-stage magnetization switching behavior will be explained with a numerical model.

4.2.2.1 Surface and Cross Section Analysis

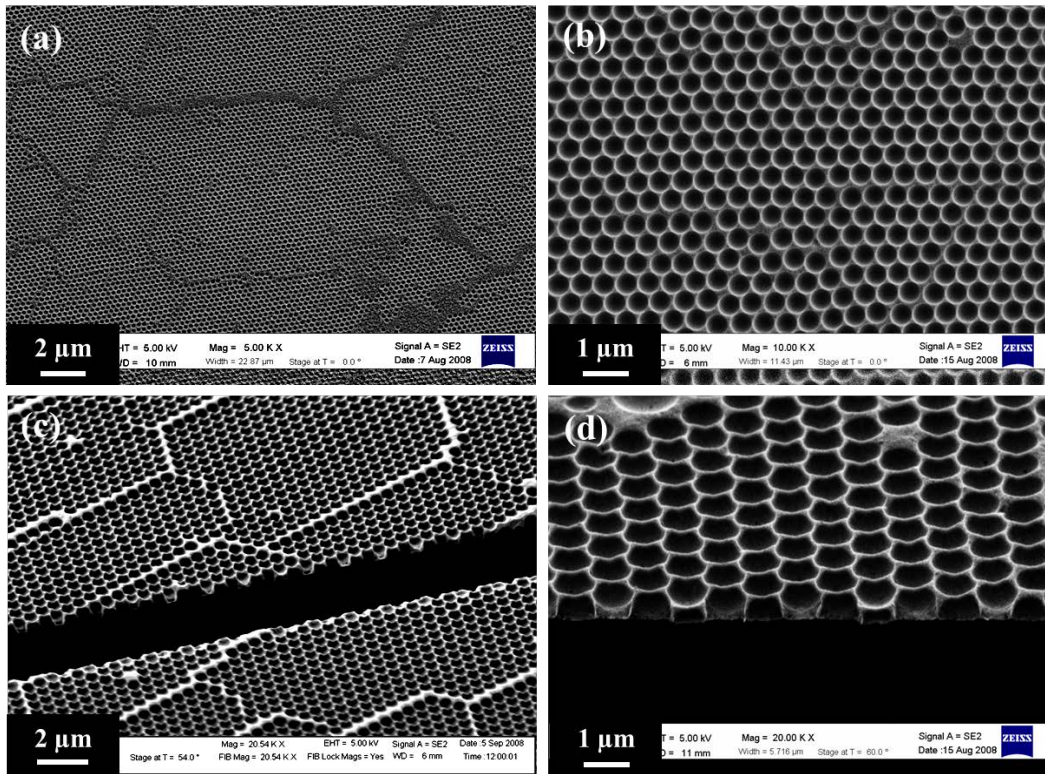


Figure 4.5 SEM images of surface and cross section of modulated substrate with top view with different scale in (a) and (b), tiled view with different scale in (c) and (d).

The surface and cross section image of modulated substrate are shown in figure 4.5. The large scale image shows the cracked part in figure 4.5 (a) and (c). However, the small scale images show the curvature surface in figure 4.5 (b) and (d).

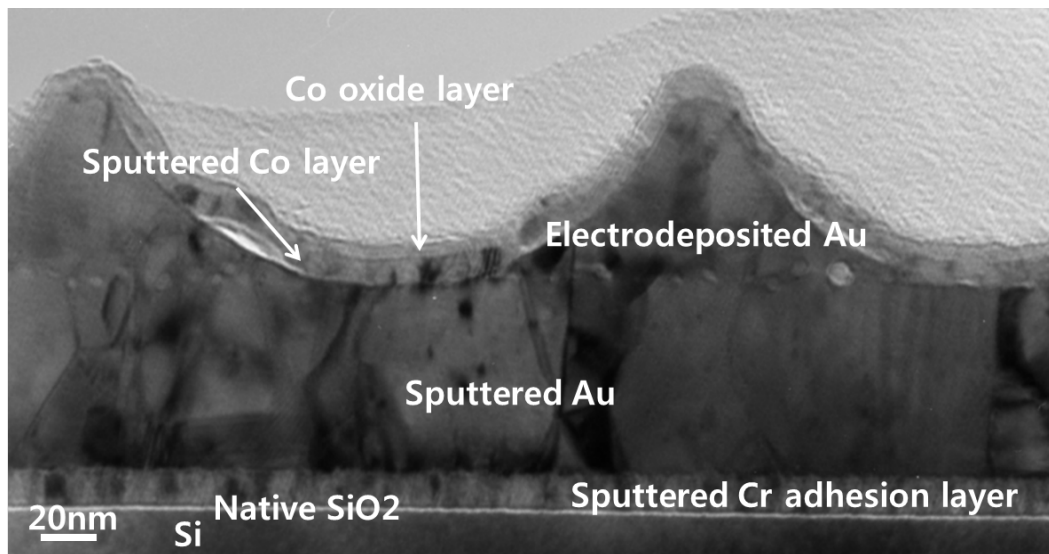


Figure 4.6 TEM image of cross section of Co/CoO bilayer on modulate substrate.

The cross section image of Co/CoO bilayer on the modulated substrate is shown in figure 4. 6. From the TEM image, it is clear that the Co/CoO bilayer is consisted with the continuation of Au surface. The Co and CoO layers are determined from TEM image. The thickness of Co and CoO layers are 8 nm and 1 nm, respectively.

4.2.2.2 M-H Hysteresis Loop Analysis

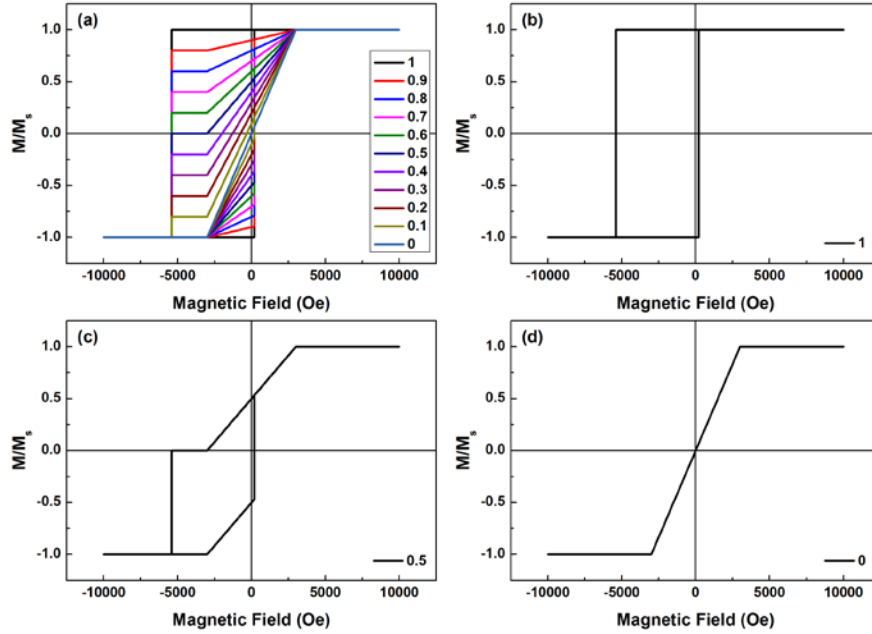


Figure 4.7 Calculated magnetic hysteresis loops depend on unbiased magnetization with (a) variety of numerical number, (b) numerical number: 1, (c) numerical number: 0.5 and (d) numerical number: 0.

The two-stage magnetization reversal depends on the perpendicular axis or parallel axis from field-cooling direction. The perpendicular axis is the easy axis for exchange bias. The parallel axis is the hard axis for exchange bias.

Based on the numerical calculation, it can be calculated from normalized magnetic hysteresis loops. It is defined as $M(\text{unbiased}) = 1 - M(\text{biased})$. If the unbiased magnetization is zero, the biased magnetization will get to 1 in figure 4.7(b). On the other hand, if the unbiased magnetization is 1, the biased magnetization will get zero from figure 4.7.(d). In this state, the remanent magnetization is zero.

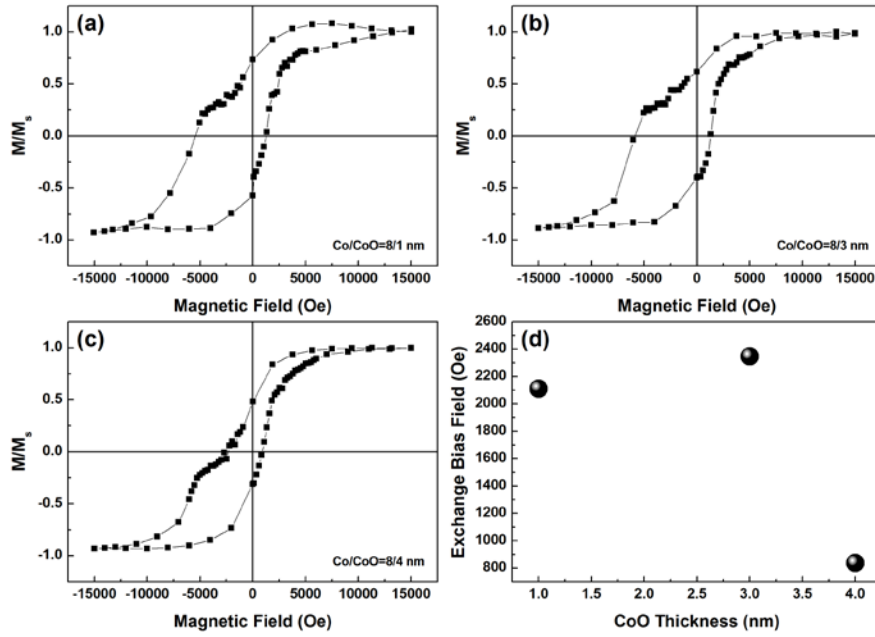


Figure 4.8 Magnetic hysteresis loops from Co/CoO bilayer on modulated substrate with different CoO thickness (a) CoO=1 nm, (b) CoO=3 nm, and (c) CoO=4 nm.

Magnetic hysteresis loops are shown in figure 4.8. When the thickness of the CoO layer is 1 nm, the measured exchange bias field is 2111 Oe. When the CoO thickness is 2 nm, the exchange bias field increased to 2347 Oe. However, when the thickness of the CoO layer is further increased to 4 nm, the exchange bias field decreased to 835 Oe. From the experimental results, the critical thickness of CoO layer is 3 nm for which maximum exchange bias field was obtained. Our results also agree with similar studies. [38]

The exchange bias is observed with two-stage switching behavior. One of the results was shown two-stage switching behavior from nano-structure. They claim that this kind of switching behavior is explained by magnetostatic interdot interaction. [39] The

magnetic domains are connected with the other domain. It will give different exchange anisotropy. On the other hand, two-stage switching has been observed in continuous films. [40] They assumed that different grain sizes of Co/CoO are formed at the surface.

From the TEM image in the figure 4.6, the surface of Au layer gives the two directions of the exchange anisotropy. Perpendicular axis is given by curvature part. Parallel axis is given by edge part. The perpendicular axis is unbiased magnetization state from field cooling due to the easy axis for magnetization reversal behavior. The parallel axis is biased magnetization state from the field cooling due to the hard axis for magnetization reversal behavior.

The total simplified exchange anisotropy energy can be expressed as,

$$E = -B \sum_i \sqrt{A_i} \cos(\theta - \phi_i - \alpha_i) + K_{AF} t_{AF} \times \sum_i \sqrt{A_i} \sin^2(3\phi_i) - H M_s t_F A_{tot} \cos(\psi - \theta) \quad (4.1)$$

The first term is the unidirectional exchange energy, followed by the magnetocrystalline energy of the antiferromagnet, and the Zeeman energy term. [6] θ , ϕ_i , α_i , and ψ are the angle of the magnetization (θ), the angle between the easy axis of the AFM easy axis and AFM surface spin (ϕ), the angle between the easy axis of the ferromagnet and antiferromagnet (α), and the direction of the applied field (ψ), respectively. From the exchange anisotropy energy equation, the magnetization vector of ferromagnetic parts is a perpendicular direction to the field cooling, their Zeeman energy is very small, and the ferromagnetic part stays pinned to the antiferromagnet part. [41] Therefore, the domain pinning region makes easier for magnetization reversal behavior.

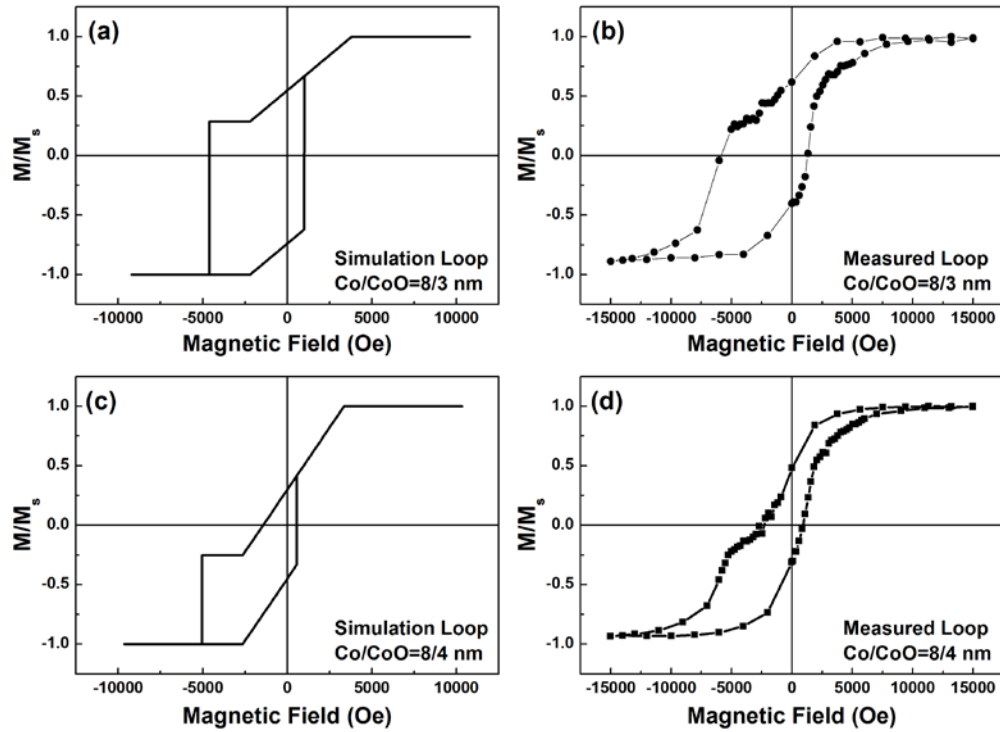


Figure 4.9 Calculation and measurement hysteresis loops from Co/CoO bilayer on modulated substrate with numerical number (a) 0.643, (c) 0.4 and thickness of Co and CoO layer (b) 8 and 3 nm, (d) 8 and 4 nm.

Based on the experiment results, magnetization hysteresis loops are calculated with experimental results. The value of unbiased magnetization is 0.643 and 0.4 from the figure 4.9 (b) and (d). Unbiased magnetization is used to calculate the magnetic hysteresis loop in figure 4.9 (a) and (c). From the calculation results, the magnetization hysteresis loops are well defined compared with experimental results.

The Co/CoO bilayer on modulated substrate has two magnetization parts for the exchange bias. It is related to biased magnetization and unbiased magnetization. Bias magnetization is related to parallel axis from the field cooling direction. On the other hand, unbiased magnetization is related to perpendicular axis from the field cooling direction.

Therefore, the origin of two-stage magnetization switching behavior is related with unbiased magnetization from calculation hysteresis loop result in figure 4.9.

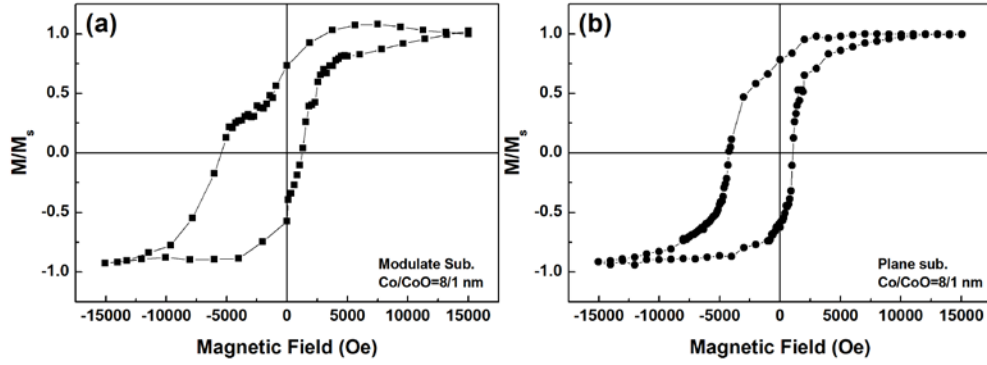


Figure 4.10 Magnetic hysteresis loops of Co/CoO=8/1 nm with (a) modulated substrate and (b) flat substrate.

The magnetization hysteresis loops are compared with Co/CoO bilayers on modulated substrate and flat substrate in the figure 4.10. Thickness of the Co and CoO layer is 8 nm and 1 nm on modulated and flat substrates, respectively. The exchange bias is measured with 2111 Oe and 1609 Oe from modulated substrate and flat substrate. Therefore, the modulated substrate system improved the exchange bias field compared to a flat substrate system.

Chapter 5

Summary and Conclusions

The physical behaviors of polycrystalline bismuth ferrite ($\text{BFO}(\text{Fe}_2\text{O}_3)$ and $\text{BFO}(\text{Fe}_3\text{O}_4)$) thin films were investigated with ferroelectric, ferromagnetic and leakage current measurement results from the $\text{BFO}(\text{Fe}_2\text{O}_3)$ and $\text{BFO}(\text{Fe}_3\text{O}_4)$ films. Based on the binding energy state results from XPS, the valence electron state of iron and oxygen was determined. From the iron, two peaks were resolved Fe^{3+} and Fe^{2+} . The oxygen peak was resolved for $\text{O}1s$ and V_{OS} . The $\text{BFO}(\text{Fe}_2\text{O}_3)$ film has larger volume of Fe^{3+} and V_{OS} states than the $\text{BFO}(\text{Fe}_3\text{O}_4)$.

The ferroelectric property is measured with AC electric field at 10 kHz. The $\text{BFO}(\text{Fe}_2\text{O}_3)$ has higher remnant polarization compared with $\text{BFO}(\text{Fe}_3\text{O}_4)$. It is related to the volume of Fe^{3+} state due to the stable state at the surface. Also the polarization direction of BFO is the (111) direction. From XRD results, the $\text{BFO}(\text{Fe}_2\text{O}_3)$ is highly oriented compare to the $\text{BFO}(\text{Fe}_3\text{O}_4)$.

The leakage current density was measured with DC electric field at room temperature. The I-V measurement result was completely different between $\text{BFO}(\text{Fe}_2\text{O}_3)$ and $\text{BFO}(\text{Fe}_3\text{O}_4)$. The $\text{BFO}(\text{Fe}_2\text{O}_3)$ film is observed higher current than the $\text{BFO}(\text{Fe}_3\text{O}_4)$ at lower electric field region. From the XPS result, $\text{BFO}(\text{Fe}_2\text{O}_3)$ film has more free carriers from the large volume of V_{OS} . On the other hand, the $\text{BFO}(\text{Fe}_3\text{O}_4)$ film is ordered by the SCLC mechanism. From the FN tunneling emission result, the $\text{BFO}(\text{Fe}_3\text{O}_4)$ is dominated by the Fe^{2+} and V_{OS} at the high electric field region.

The magnetic hysteresis loop is measured at room temperature. The $\text{BFO}(\text{Fe}_3\text{O}_4)$ film has larger magnetization than $\text{BFO}(\text{Fe}_2\text{O}_3)$. The magnetization of BFO films depend on the valence electron state of Fe. The $\text{BFO}(\text{Fe}_3\text{O}_4)$ film has larger volume of Fe^{2+} at the surface. It increases the magnetization compared with $\text{BFO}(\text{Fe}_2\text{O}_3)$.

Exchange bias behavior of Co/CoO bilayer is studied with flat and modulated substrates. From the results of Co/CoO bilayer on flat substrate, the magnetization is fully biased by the field-cooling process even for different thickness of Co layer. The uniaxial exchange anisotropy is measured by the field-cooling process. The training effect is measured with cycling magnetization hysteresis loop measurement after the field-cooling process. The exchange bias field decreases with increasing measurement times. The decreasing of exchange bias field is related to the decreasing domain-wall pinning regions.

The exchange bias behavior of Co/CoO bilayer on modulated substrate is studied with numerical calculation and magnetization hysteresis loops. The curvature surface of Co/CoO bilayer has perpendicular and parallel axis that contribute differently to the magnetization reversal behavior. Based on thin film study, when the magnetic field is perpendicular to the Co/CoO interface the resulting hysteresis loop is unbiased. Conversely, when the Co/CoO interface is measured parallel to the magnetic field it results in biased magnetization hysteresis loop. The two-stage magnetization hysteresis loop is observed from the Co/CoO bilayer on modulated substrate. The calculated results further conform the unbiased and biased magnetization are directly related to the perpendicular and parallel axis. More detail study for the exchange bias behavior from Co/CoO bilayer on modulated substrate need to understand with domain-wall motion.

References

1. Charles Kittel, "Introduction to Solid State Physics Eighth Edition", John Wiley & Sons, Inc (2005).
2. James F. Scott, "Ferroelectric Memories", Springer (2000).
3. R. Ramesh, "Thin Film Ferroelectric Materials and Devices (Electronic Materials: Science & Technology)", Springer (2014).
4. Nicola A. Spaldin, "Magnetic Material : Fundamentals and Applications", Cambridge University Press (2011).
5. J. M. D. Coey, "Magnetism and Magnetic Materials", Cambridge University Press (2010).
6. J. Nogues, Ivan K. Schuller, "Exchange bias", Journal of Magnetism and Magnetic Materials, (1999) 192, 203.
7. J. Nogues, J. Sort, V. Langlais, V. Skumryev, S. Surinach, J. S. Musoz, M. D. Baro, "Exchange bias in nanostructures". Physics Reports (2005) 422, 65.
8. J. Wang, J. B. Neaton, H. Zheng, V. Nagarajan, S. B. Ogale, B. Liu, D. Viehland, V. Vaithyanathan, D. G. Schlom, U. V. Waghmare, N. A. Spaldin, K. M. Rabe, M. Wuttig and R. Ramesh, "Epitaxial BiFeO₃ multiferroic thin film heterostructures", Science (2003) 229, 1719.
9. P. Ravindran, R. Vidya, A. Kjekshus, H. Fjellvåg, and O. Eriksson, "Theoretical investigation of magnetoelectric behavior in BiFeO₃", Physical Review B (2006) 74, 224412.
10. J. B. Neaton, C. Ederer, U. V. Waghmare, N. A. Spaldin, and K. M. Rabe, "First-principles study of spontaneous polarization in multiferroic BiFeO₃", Physical Review B (2005) 71, 014113.

11. C. Ederer, and N. A. Spaldin, "Weak ferromagnetism and magnetoelectric coupling in bismuth ferrite", *Physics Review B* (2005) 71, 060401(R).
12. S. Cui, G. Hu, W. Wu, C. Yang, L. Jiao, and Z. Wen, "Aging-Induced Double Ferroelectric Hysteresis Loops and Asymmetric Coercivity in As-Deposited $\text{BiFe}_{0.95}\text{Zn}_{0.05}\text{O}_3$ Thin Film", *J. Am. Ceram. Soc.*, (2009) 92, 1610.
13. G. L. Yuan, Y. Yang, and S. W. Or, "Aging-induced double ferroelectric hysteresis loops in BiFeO_3 multiferroic ceramic", *Applied Physics Letters*, (2007) 91, 122907.
14. W. Eerenstein, F. D. Morrison, J. Dho, M. G. Blamire, J. F. Scott, and N. D. Mathur, "Comment on Epitaxial BiFeO_3 Multiferroic Thin Film Heterostructures", *Science* (2005) 307, 1203.
15. J. Wang, J. B. Neaton, H. Zheng, V. Nagarajan, S. B. Ogale, B. Liu, D. Viehland, V. Vaithyanathan, D. G. Schlom, U. V. Waghmare, N. A. Spaldin, K. M. Rabe, M. Wuttig and R. Ramesh, "Response to Comment on Epitaxial BiFeO_3 multiferroic thin film heterostructures", *Science* (2005) 307, 1203.
16. H. I. Choi, S. W. Kim, J. W. Kim, D. Do, S. S. Kim, W. J. Kim, M. H. Lee, J. S. Park, H. J. Cho, D. J. Kim, J. H. Cho, and T. K. Song, "Thickness-dependent ferroelectric behaviors of (111)-textured polycrystalline pseudo-cubic BiFeO_3 thin films", *J. Korean Phys. Soc.* **60**, 288 (2012).
17. J. Chen, X. Xing, A. Watson, W. Wang, R. Yu, J. Deng, L. Yan, C. Sun, and X. Chen, "Rapid Synthesis of Multiferroic BiFeO_3 Single-Crystalline Nanostructures", *Chemical Matter* (2007) 19, 3598.
18. P. Li, Y-H. Lin, and C-W. Nan, "Effect of nonmagnetic alkaline-earth dopants on magnetic properties of BiFeO_3 thin films", *Journal of Applied Physics* (2011) 110, 033922.

19. X. Wang, G. Hu, L. Cheng, C. Yang, and W. Weibing, "Large Piezoelectric Coefficient in Tb-Doped BiFeO₃ Films", *Applied Physics Letter* (2011) 99, 262901
20. F. Yan, M-O. Lai, L. Lu, and T-J. Zhu, "Enhanced multiferroic properties and valence effect of Ru-doped BiFeO₃ thin films", *Journal of Physical Chemistry C* (2010) 114,6994
21. F. Yan, T-J. Zhu, M-O. Lai, and L. Lu, "Influence of La and Ru dopants on multiferroic properties of polycrystalline BiFeO₃ thin films", *Applied Physics Express* (2010) 4, 111502.
22. M. A. Lampert, "Simplified theory of space-charge-limited currents in an insulator with traps", *Physics Review* (1956) 103, 1648.
23. T. Kawae, Y. Tereuchi, H. Tsuda, M. Kumeda, and A. Morimoto, "Improved leakage and ferroelectric properties of Mn and Ti codoped BiFeO₃ thin films", *Applied Physics Letter* (2007) 94, 112904.
24. H. Yang, M. Jain, N. A. Suvorova, H. Zhou, H. M. Luo, D. M. Feldmann, P. C. Dowden, R. F. DePaula, S. R. Foltyn and Q. X. Jia, "Temperature-dependent leakage mechanisms of Pt/BiFeO₃/SrRuO₃ thin film capacitors", *Applied Physics Letter* (2007) 91, 072911.
25. J. Wu, J. Wang, D. Xiao, and J. Zhu, "Leakage mechanism of cation-modified BiFeO₃ thin film", *AIP Advanced* (2012) 1, 022138.
26. G. W. Pabst, L. W. Martin, Y-H. Chu, and R. Ramesh, "Leakage mechanism in BiFeO₃ thin films", *Applied Physics Letter* (2007) 90, 072902.
27. H. Naganuma, and S. Okamura, "Structural, magnetic, and ferroelectric properties of multiferroic BiFeO₃ film fabricated by chemical solution deposition", *Journal of Applied Physics* (2007) 101, 09M103.

28. X. Qi, J. Dho, R. Tomov, M. G. Blamire, and J. L. MacMaus-Driscoll, "Greatly reduced leakage current and conduction mechanism in aliovalent-ion-doped BiFeO₃", *Applied Physics Letters* (2005) 86, 062903.
29. H. Yang, Y. Q. Wang, H. Wang, and Q. X. Jia, "Oxygen concentration and its effect on the leakage current in BiFeO₃ thin films", *Applied Physics Letters* (2010) 96, 012909.
30. F. Yan, T-J. Zhu, M-O. Lai, and L. Lu, "Enhanced multiferroic properties and domain structure of La-doped BiFeO₃ thin films", *Scripta Materialia* (2010) 63, 780.
31. W. H. Meiklejohn, and C. P. Bean, "New Magnetic Anisotropy", *Physical Review* (1956) 102, 1413.
32. R. L. Stamps, "Mechanism for exchange bias", *Journal of Physics D:Applied Physics* (2000) 33, R247.
33. T. Gredig, I. N. Krivorotove, and E. D. Dahlberg, "Magnetization reversal in exchange biased Co/CoO probed with anisotropic magnetoresistance", *Journal of Applied Physics* (2002) 91, 7760.
34. J. Y. Yi, C. L. Platt, M. L. Rudee, A. E. Berkowitz, and T. L. Cheeks, "Sputter deposited Co/CoO composite materials" *Journal of Applied Physics* (1996) 79, 5072.
35. T. Gredig, I. N. Krivorotove, P. Eames, and E. D. Dahlberg, "Unidirectional coercivity enhancement in exchange-biased Co/CoO" *Applied Physics Letters* (2002) 81, 1270.
36. F. Radu, M. Etzkorn, R. Siebrecht, T. Schmitte, K. Westerholt, and H. Zabel, "Interfacial domain formation during magnetization reversal in exchange-biased CoO/Co bilayers", *Physical Review B* (2003) 67, 134409.

37. E. Menendez, T. Dias, J. Geshev, J. F. Lopez-Barbera, J. Nogues, R. Steitz, B. J. Kirby, J. A. Borchers, L. M. C. Pereira, A. Vantomme, and K. Temst, "Interdependence between training and magnetization reversal in granular Co-CoO exchange bias systems", *Physical Review B* (2014) 89, 144407.
38. T. Gredig, I. N. Krivorotov, and E. D. Dahlberg, "Temperature dependence of magnetization reversal and angular torque in Co/CoO", *Physical Review B* (2006) 74, 094431.
39. E. Girgis, R. D. Portugal, H. Loosvelt, M. J. Van-Bael, I. Gordon, M. Malfait, K. Temst, and C. V. Haesendonck, "Enhanced Asymmetric Magnetization Reversal in Nanoscale Co/CoO Arrays: Competition between Exchange Bias and Magnetostatic Coupling", *Physical Review Letters* (2003) 91, 187202.
40. R. Wu, J. Z. Wei, X. L. Peng, J. B. Fu, S. Q. Liu, Y. Zhang, Y. H. Xia, C. S. Wang, Y. C. Yang, and J. B. Yang, "The asymmetric magnetization reversal in exchange biased granular Co/CoO films", *Applied Physics Letters* (2014) 104, 182403.
41. A. N. Dobrynin, D. N. Ievlev, C. Hendrich, K. Temst, P. Lievens, U. Hormann, J. Verbeeck, G. Van Tendeloo, A. Vantomme, "Influence of finite size effects on exchange anisotropy in oxidized Co nanocluster assembled films", *Physics Review B* (2006) 73, 245416.

Biographical Information

After completing high school in his native country of Korea, Choi Hai In pursued his college education in Changwon, Korea. He then received his Bachelor's Degree in Science from Changwon National University, Changwon in Korea. He then worked as a student at Changwon National University for one and half years during the Master Program. Mr. Choi was also involved in the Functional Oxide Thin Film Lab in Changwon National University. After a certain period of time, he attended the double master degree program between Changwon National University and University of Texas at Arlington in Physics Department.